Journal of Computational Physics 229 (2010) 5653–5691

Contents lists available at ScienceDirect

Journal of Computational Physics

journal homepage: www.elsevier.com/locate/jcp

Explicit Runge–Kutta residual distribution schemes for time dependent problems: Second order case

M. Ricchiuto *, R. Abgrall

INRIA Bordeaux, Sud-Ouest, équipe BACCHUS, 351, Cours de la Libération, 33405 Talence cedex, France

ARTICLE INFO

Article history:
Received 23 July 2009
Received in revised form 1 April 2010
Accepted 1 April 2010
Available online 13 April 2010

Keywords:
Hyperbolic conservation laws
Time dependent problems
Second order schemes
Explicit schemes
Residual distribution
Runge–Kutta time-stepping

ABSTRACT

In this paper, we construct spatially consistent explicit second order discretizations for time dependent hyperbolic problems, starting from a given residual distribution (RD) discrete approximation of the steady operator. We review the existing knowledge on consistent RD mass matrices and highlight the relations between different definitions. We then introduce our explicit approach which is based on three main ingredients: first recast the RD discretization as a stabilized Galerkin scheme, then use a shifted time discretization in the stabilization operator, and lastly apply high order mass lumping on the Galerkin component of the discretization. The discussion is particularly relevant for schemes of the residual distribution type [18,3] which we will use for all our numerical experiments. However, similar ideas can be used in the context of residual-based finite volume discretizations such as the ones proposed in [14,12]. The schemes are tested on a wide variety of classical problems confirming the theoretical expectations.

1. Introduction

The aim of this study is to understand how to construct fully explicit consistent discretizations for time dependent problems, given a *residual-based* discretization of steady limit of a hyperbolic conservation law. As a case study we consider schemes of the residual distribution (RD) type [18,3]. While well understood in the steady case, their formulation in the time dependent case is not completely clear, due to the lack of a rigorous formulation allowing a natural extension. In particular, the lack of sufficient constraints on the discretization has led in time to a number of different formulations all featuring different mass matrices [9,22,19,20]. In this paper, we show that all these formulations can be obtained from one another by adding/subtracting a properly defined dissipation operator. We also show the existence of entire families of additional consistent mass matrices.

Next, we show how to combine all of the above discretization with high order (second order) mass lumping to obtain fully explicit schemes. This is done in three steps: first rewriting the RD discretization as a stabilized Galerkin scheme, then using a shifted time operator in the stabilization, and lastly applying high order mass lumping on the Galerkin component of the discretization. Note that in the case of nonlinear RD discretizations based on second order time integration in time, positivity preservation is obtained only under an explicit CFL-type condition [4,18]. This fact, related to the properties of the underlying ODE integrator [8], and the highly implicit nature of the schemes leads to poor efficiency. The explicit formulation proposed here is one possible solution to this issue.

The work discussed here somehow generalizes the initial work of [35] where only central Lax-Wendroff type discretizations are considered. Moreover, in the paper we will show that the ideas presented here also apply to other classes of schemes, such as the ones proposed in [14].

* Corresponding author. Tel.: +33 5 24 57 41 17; fax: +33 5 24 57 40 38.
E-mail addresses: Mario.Ricchiuto@inria.fr (M. Ricchiuto), Remi.Abgrall@inria.fr (R. Abgrall).

0021-9991/$ - see front matter © 2010 Elsevier Inc. All rights reserved.
doi:10.1016/j.jcp.2010.04.002

The structure of the paper is as follows. We start by introducing the notations used throughout the discussion. Then, in Section 3 we review different formulations of RD for time dependent problems. We discuss their relations, and show how several families of consistent formulations exist. The new explicit schemes we propose are presented in Section 4. In particular, the three main steps mentioned above are described in Sections 4.1, 4.2, and 4.3, while in Section 4.4 we give some more details on the final form of the different discretizations obtained. A summary of the different numerical schemes that we use in the numerical tests is given in Section 5, while the results of these tests are discussed in Sections 6 and 7. We end the paper with some conclusive remarks and some thoughts for further developments.

2. Mathematical problem and notation

We seek approximations of solutions of the time dependent hyperbolic problem

$$r(u) = 0 \quad \text{with} \quad r(u) = \partial_t u + \nabla \cdot \boldsymbol{\mathcal{F}}(u) \tag{1}$$

on some spatial domain Ω, and on some temporal domain $[0, t_f]$. We will mainly focus on the two-dimensional case $\Omega \in \mathbb{R}^2$, but the generalization to three spatial dimensions is trivial.

We discretize Ω by an unstructured triangulation denoted by $\mathcal{T}_h$, with T denoting the generic element of the mesh, and h the mesh parameter (characteristic mesh size). When no confusion is generated we denote the nodes of T by {1, 2, 3}. In every element, we denote by $\vec{n}_j$ the inward pointing vector normal to the edge facing node j, scaled by the length of the edge. Denoting by φ_i the P^1 Lagrange basis function corresponding to node $i \in \mathcal{T}_h$, we have

$$\nabla \varphi_i|_T = \frac{\vec{n}_i}{2|T|}. \tag{2}$$

The P^1 approximation of u will be denoted by u_h, and it is given by

$$u_h = \sum_{i \in \mathcal{T}_h} u_i \varphi_i = \sum_{T \in \mathcal{T}_h} \sum_{j \in T} u_j \varphi_j|_T. \tag{3}$$

The temporal domain is discretized by a set of non-overlapping time slabs $[t^n, t^{n+1}]$. We denote by $\Delta t = t^{n+1} - t^n$ the time step.

To simplify the presentation of the next sections we also introduce here the *element fluctuation* defined as

$$\phi(u_h) = \int_T \nabla \cdot \boldsymbol{\mathcal{F}}_h(u_h) dx\, dy = \oint_{\partial T} \boldsymbol{\mathcal{F}}_h(u_h) \cdot \hat{n} dl, \tag{4}$$

the *element residual*

$$\Phi(u_h) = \int_T r(u_h) dx\, dy = \int_T (\partial_t u_h + \nabla \cdot \boldsymbol{\mathcal{F}}_h(u_h)) dx\, dy = \sum_{j \in T} \frac{|T|}{3} \frac{du_j}{dt} + \phi(u_h) \tag{5}$$

and the local Galerkin residual

$$\phi_i^{\mathrm{G}}(u_h) = \int_T \varphi_i \nabla \cdot \boldsymbol{\mathcal{F}}_h(u_h) dx\, dy. \tag{6}$$

In the expressions above u_h represents the P^1 numerical approximation of the unknown, and $\boldsymbol{\mathcal{F}}_h(u_h)$ a discrete approximation of the flux. Note that all of the above quantities depend on time via u_h. To simplify the notation, we do not introduce a super- or sub-script indicating the element T over which they are evaluated, this being always clear from the context.

3. Second order RD: the proliferation of mass matrices

Let us for the moment consider the particular case of (1) given by the linear constant advection problem

$$\partial_t u + \vec{a} \cdot \nabla u = 0. \tag{7}$$

We focus our attention on discrete counterparts of (7) that, on a slab $\mathcal{T}_h \times [t^n, t^{n+1}]$ can be written as

$$\sum_{T | i \in T} \left\{ \sum_{j \in T} m_{ij}^T \frac{du_j}{dt} + \beta_i \phi(u_h) \right\} = 0 \quad \forall i \in \mathcal{T}_h. \tag{8}$$

Last definitions give a scheme that requires the solution of a (generally) nonlinear system if the *mass matrix* m_{ij} is non-diagonal. Moreover, introducing the *nodal residuals*

$$\Phi_i(u_h) = \sum_{j \in T} m_{ij}^T \frac{du_j}{dt} + \beta_i \phi(u_h) \tag{9}$$

we also require that

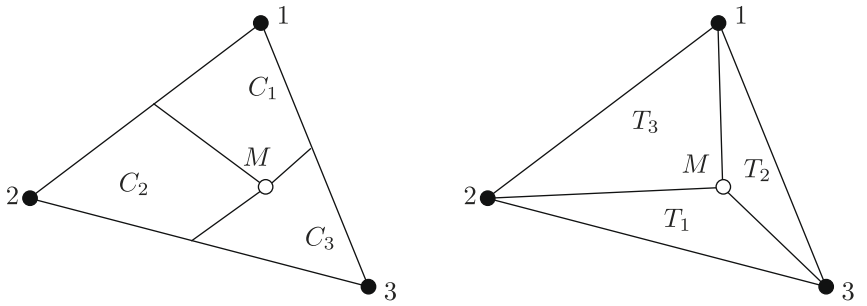

Fig. 1. (Left) Formulation 3: dual areas C_j, $|C_j| = \beta_j|T|$. (Right) Formulation 4: area coordinates of the distribution point M; $|T|_j = \beta_j|T|$.

$$\sum_{j\in T} \Phi_j(u_h) = \Phi(u_h) \tag{10}$$

with $\Phi(u_h)$ given by (5).

The prototype (8) is meant to be a consistent generalization to the time dependent case of the *fluctuation splitting/residual distribution* discretization which approximates the steady limit of (7) as

$$\sum_{T|i\in T} \beta_i \phi(u_h) = 0 \quad \forall i \in \mathcal{T}_h \tag{11}$$

with

$$\sum_{j\in T} \beta_j = 1. \tag{12}$$

In order to distinguish the steady advective operator from the time dependent equation, we have chosen to keep a distinction between the fluctuation (4) and the residual (5), the latter representing the integral of the whole equation.

Historically, the first consistent constructions to obtain such a generalization were based on two different points of view. In the first approach [10,9], one simply replaces the fluctuations in the discrete equations (11) with the full residual (5). This residual is then distributed exactly as in (11) (with the LDA scheme in the original reference [10,9,18]), leading to

$$0 = \sum_{T|i\in T} \beta_i \Phi(u_h) = \sum_{T|i\in T} \left(\sum_{j\in T} m_{ij}^{\mathrm{F1}} \frac{du_j}{dt} + \beta_i \phi(u_h) \right), \quad m_{ij}^{\mathrm{F1}} = \frac{|T|}{3}\beta_i \tag{13}$$

with δ_{ij} Kronecker's delta, and F1 standing for Formulation 1.

A second approach [29,22] uses an analogy with stabilized Galerkin finite element schemes in which the discrete equations (11) are obtained as

$$\sum_{T|i\in T} \beta_i \phi(u_h) = \sum_{T|i\in T} \phi_i^{\mathrm{G}}(u_h) + \sum_{T|i\in T} \delta\phi_i = \int_\Omega \varphi_i \vec{a}\cdot\nabla u_h dx\,dy + \sum_{T|i\in T} \int_T \delta_{\varphi_i} \vec{a}\cdot\nabla u_h dx\,dy$$

with the perturbation to the test function δ_{φ_i} depending on the distribution coefficients β_i. In particular, for constant advection and a P^1 variable approximation, one can assume δ_{φ_i} to be a constant, to find easily (in two space dimensions) $\delta_{\varphi_i}|_T = \beta_i - 1/3$. In the time dependent case this naturally leads to

$$0 = \int_\Omega \varphi_i r(u_h) dx\,dy + \sum_{T|i\in T} \int_T \delta_{\varphi_i} r(u_h) dx\,dy = \sum_{T|i\in T} \left(\sum_{j\in T} m_{ij}^{\mathrm{F2}} \frac{du_j}{dt} + \beta_i \phi(u_h) \right), \quad m_{ij}^{\mathrm{F2}} = \frac{|T|}{36}(3\delta_{ij} + 12\beta_i - 1) \tag{14}$$

with δ_{ij} Kronecker's delta, and F2 standing for Formulation 2.

A different approach has instead been proposed in [20], where the authors use the idea that in every $T \in \mathcal{T}_h$ the combination of terms arising from the multiplication of the mass matrix with the nodal time derivatives should give back an integral of the time derivative of u_h over a dual sub-element $C_j \in T$. Consistency is guaranteed by the requirement $|C_j| = \beta_j|T|$.[1] In particular, in the paper the authors require *the node j to belong to* C_j (cf. Fig. 1). Conditions for second order of accuracy are shown to be

$$\sum_{i\in T} m_{ij} = \frac{|T|}{3}, \quad \sum_{j\in T} m_{ij} = |T|\beta_i. \tag{15}$$

[1] Which implicitly assumes $\beta_i \geqslant 0\ \forall i$.

In the reference, the authors ultimately arrive to the following formulation

$$0 = \sum_{T|i\in T} \int_{T_i} r(u_h)dx\,dy = \sum_{T|i\in T} \left(\sum_{j\in T} m_{ij}^{\mathrm{F3}} \frac{du_j}{dt} + \beta_i \phi(u_h) \right), \quad m_{ij}^{\mathrm{F3}} = \frac{|T|}{3}\beta_i(\delta_{ij} + 1 - \beta_j) \tag{16}$$

with δ_{ij} Kronecker's delta, and F3 standing for Formulation 3. This formulation is proposed mainly for schemes with a multidimensional upwind character [18], and in particular for those schemes that, when the advection speed points toward an edge of element T, give $\beta_j \geqslant 0$ only if j belongs to this edge. In this case, only the rows of m_{ij}^{F3} relative to these nodes contain non-zero elements.

The idea of [20] can actually be used to derive still another member to the family of consistent mass matrices. It suffices to follow the exact same developments of the reference, except that now we consider the sub-cell C_j to be a triangle that *does not contain node j*. In particular, whenever $\beta_i \geqslant 0\ \forall i$, we note that we can find a unique point, say $M \in T$, such that $\varphi_i(M) = \beta_i\ \forall i$. This means that the β_i coefficients represent the area coordinates of M (see Fig. 1). With the notation of Fig. 1, using the fact that $u_h(M) = \beta_1 u_1 + \beta_2 u_2 + \beta_3 u_3$ we find in the time dependent case:

$$0 = \sum_{T|i\in T} \int_{T_i} r(u_h)dx\,dy = \sum_{T|i\in T} \left(\sum_{j\in T} m_{ij}^{\mathrm{F4}} \frac{du_j}{dt} + \beta_i^T \phi(u_h) \right), \quad m_{ij}^{\mathrm{F4}} = \frac{|T|}{3}\beta_i(1 - \delta_{ij} + \beta_j) \tag{17}$$

with δ_{ij} Kronecker's delta, and F4 standing for Formulation 4. Note that the difference with respect to the matrix proposed in [20] is that here $j \notin T_j$. One easily checks that conditions (15) are verified.

All of the above construction can be still generalized by noting that, given the distribution coefficients β_i^T, the only constraints available are given by (15). These constraints actually correspond to the conservation requirement (10), and to the requirement that, whenever the differential operator

$$r(u_h) = \partial_t u_h + \vec{a}\cdot\nabla u_h$$

is (as in the steady case) locally constant, say $r(u_h)|_T = r^T$, then

$$\Phi_i = \beta_i^T |T| r^T.$$

These properties are always verified if we can find a Petrov–Galerkin test function ω_i such that on every T

$$\Phi_i(u_h) = \int_T \omega_i r(u_h)dx\,dy \tag{18}$$

with

$$\sum_{j\in T} \omega_j = 1, \quad \frac{1}{|T|}\int_T \omega_i dx\,dy = \beta_i^T. \tag{19}$$

As we will show later, the formal second order of accuracy is guaranteed as long as ω_i is locally bounded. Note also that

$$m_{ij}^T = \int_T \omega_i \varphi_j dx\,dy. \tag{20}$$

The number of functions that verify these constraints is infinite. For example, to obtain the formulation F1 (cf. equation (13)) one can choose on each T

$$\omega_i^{\mathrm{F1}}|_T = \beta_i^T \chi_T$$

having denoted by χ_T the characteristic function

$$\chi_T(x,y) = \begin{cases} 1 & \text{if } (x,y) \in T. \\ 0 & \text{if } (x,y) \notin T. \end{cases}$$

Conversely, formulation F2 (cf. equation (14) is obtained for

$$\omega_i^{\mathrm{F2}} = \varphi_i + \sum_{T|i\in T} \delta_{\varphi_i}\chi_T.$$

Formulations F3 and F4 are instead obtained by taking for example (cf. equations (16) and (17))

$$\omega_i^{\mathrm{F3/F4}}|_T = \chi_{C_i}.$$

Moreover, for any given test function ω_i verifying all the consistency, conservation, and accuracy constraints, we can easily come up with a modified function, say $\tilde{\omega}_i$ with all the desirable properties. For example, if we can find three bounded functions, say f_1, f_2, and f_3 such that

$$\sum_{j=1}^{3} f_j = c_f$$

with c_f a constant, we can modify ω_i as follows:

$$\bar{\omega}_i = \omega_i + K(f_i - \bar{f}_i), \quad \bar{f}_i = \frac{1}{|T|}\int_T f_i \, dx\, dy \tag{21}$$

with K an arbitrary parameter! Note that this term does not affect consistency or conservation, due to the fact that (using for the nodes of T the local renumbering $\{i,j,k\} \to \{1,2,3\}$)

$$\sum_{j=1}^{3}(f_j - \bar{f}_j) = 0, \quad \int_T (f_j - \bar{f}_j) dx\, dy = 0$$

nor it does pollute the accuracy of the discretization, as long as the each f_i is bounded. Moreover, in the P^1 case ∇u_h is constant per element, hence

$$\int_T (f_j - \bar{f}_j)\vec{a}\cdot\nabla u_h \, dx\, dy = 0$$

so that the extra term only affects the form of the mass matrix. This leads clearly to quite a large number of consistent mass matrices, and extra constraints are needed to make sure one does the right thing.

Remark 3.1 (*Accuracy and stability*). Note that all of the above discretizations can be though as Petrov–Galerkin schemes where the nodal equations are obtained as

$$\int_\Omega \omega_i r(u_h) = 0 \quad \forall i \in \mathcal{T}_h$$

with a locally differentiable test function ω_i. As a consequence, all of them have a *residual character* (if $r(u_h) = 0$, u_h is a solution of the discrete equations). Nevertheless, a stability criterion would be needed to allow to rule out some of these matrices. Unfortunately, few tools are available to analyze the stability of RD schemes, coercivity and/or energy estimates not being available. A Fourier analysis of the different mass matrix formulations is under way to clarify this aspect. This aspect is left out of the discussion of this paper, which mainly focuses on the formal accuracy of the schemes.

Before going on to the construction of explicit schemes, we make the following observation. Let us take $f_i = \varphi_i$ in (21). In this case we have

$$\bar{f}_i = \bar{\varphi}_i = \frac{1}{|T|}\int_T \varphi_i = \frac{1}{3}.$$

So, according to (21), any mass matrix can be modified as

$$\tilde{m}^T_{ij} = m^T_{ij} + K\int_T (\varphi_i - \bar{\varphi}_i)\varphi_j \, dx\, dy = \int_T \omega_i\varphi_j \, dx\, dy + K\int_T (\varphi_i - \bar{\varphi}_i)\varphi_j \, dx\, dy$$

that leads to the semi-discrete scheme

$$\sum_{T|i\in T}\left(\sum_{j\in T}\left(m^T_{ij} + K\delta m_{ij}\right)\frac{du_j}{dt} + \beta_i\phi(u_h)\right) = 0, \quad \delta m_{ij} = \frac{|T|}{36}(3\delta_{ij} - 1) \tag{22}$$

with δ_{ij} Kronecker's delta. As already noted in [32], the matrix δm_{ij} is symmetric, and defines a dissipation operator, that is

$$v^T[\delta m_{ij}]v \geqslant 0, \quad \forall v \in \mathbb{R}^3.$$

In the last reference, this term has been used to provide further stabilization to a nonlinear second order variant of a Lax-Friedrich's scheme. It is worth noting that comparing (13) and (14) with (22), one immediately sees that

$$m^{F2}_{ij} = m^{F1}_{ij} + \delta m_{ij}. \tag{23}$$

The third and first formulations are linked by a very similar relation:

$$m^{F3}_{ij} = m^{F1}_{ij} + \widetilde{\delta m}_{ij}, \quad \widetilde{\delta m}_{ij} = \frac{|T|}{3}\left(\beta_i\delta_{ij} - \beta_i\beta^T_j\right), \tag{24}$$

where, *provided that* $\beta_i \geqslant 0$ $\forall i$, then the symmetric matrix $\widetilde{\delta m}_{ij}$ also defines a dissipation operator. In particular, $\forall v \in \mathbb{R}^3$ we have

$$v^T[\widetilde{\delta m}_{ij}]v = \frac{|T|}{3}\beta^T_1\beta^T_2(v_1 - v_2)^2 + \frac{|T|}{3}\beta^T_1\beta^T_3(v_1 - v_3)^2 + \frac{|T|}{3}\beta^T_3\beta^T_2(v_3 - v_2)^2 \geqslant 0.$$

A similar relation holds for the last formulation, only this time we have

$$m_{ij}^{\mathrm{F1}} = m_{ij}^{\mathrm{F4}} + \widetilde{\delta m}_{ij}. \tag{25}$$

This last relation allows finally to show that *all the formulations can be obtained from one another by adding/subtracting a properly defined dissipation operator*:

$$\begin{aligned} m_{ij}^{\mathrm{F1}} &= m_{ij}^{\mathrm{F4}} + \widetilde{\delta m}_{ij}, \\ m_{ij}^{\mathrm{F2}} &= m_{ij}^{\mathrm{F1}} + \delta m_{ij} = m_{ij}^{\mathrm{F4}} + \widetilde{\delta m}_{ij} + \delta m_{ij}, \\ m_{ij}^{\mathrm{F3}} &= m_{ij}^{\mathrm{F1}} + \widetilde{\delta m}_{ij} = m_{ij}^{\mathrm{F4}} + 2\widetilde{\delta m}_{ij}. \end{aligned} \tag{26}$$

Remark 3.2. The last relations show that, for a fixed approximation of the advection operator, the formulation F4 is the least dissipative of all. Nevertheless, a formal stability analysis is still needed to clarify this aspect (cf. Remark 3.1).

Remark 3.3. In one space dimension, if the spatial discretization is given by the classical 1d upwind scheme, the formulations F1, F3, and F4 become identical. The formulation F2, instead, reduces to the 1D SUPG scheme obtained by defining the τ SUPG parameter as [28,37,24]

$$\tau = \frac{\Delta x}{2|a|}.$$

4. Construction of explicit schemes

We present here the construction of consistent explicit variants of RD schemes, based on Runge–Kutta time-stepping. The construction consists of three steps:

1. Rewriting RD as a stabilized Galerkin discretization.
2. Use of a shifted time discretization in the stabilization term.
3. Introduction of high order mass lumping.

These three steps are described in the following sections.

4.1. Bubble stabilization

We start by assuming that, however complex the definition of the β_i coefficients and of the mass matrix, there exists a uniformly bounded and locally differentiable function γ_i such that we can rewrite the (8) as

$$\int_\Omega \varphi_i(\partial_t u_h + \vec{a}\cdot\nabla u_h)dx\,dy + \sum_{T|i\in T}\int_T \gamma_i(\partial_t u_h + \vec{a}\cdot\nabla u_h)dx\,dy = 0, \tag{27}$$

where γ_i plays the role of a "stabilizing" bubble function, and satisfies

$$\begin{cases} \sum_{j\in T}\gamma_j = 0, \\ \int_T(\varphi_i+\gamma_i)\partial_t u_h dx\ dy = \sum_{j\in T} m_{ij}\frac{du_j}{dt}, \\ \frac{1}{|T|}\int_T(\varphi_i+\gamma_i)dx\ dy = \beta_i. \end{cases} \tag{28}$$

The last three relations guarantee the satisfaction of the conservation property, and of the consistency with the (given) spatial discretization, so that ultimately (cf. equation (9))

$$\Phi_i(u_h) = \sum_{j\in T} m_{ij}\frac{du_j}{dt} + \beta_i\phi(u_h) = \int_T \varphi_i r(u_h)dx\,dy + \int_T \gamma_i r(u_h)dx\,dy. \tag{29}$$

Note that, for our scopes, *it is not necessary to actually show particular forms of such functions which, as we shall see in the following, are just an artifact allowing to analyze the accuracy of the schemes proposed in the paper*. Nevertheless, whenever we can exhibit the existence of a Petrov–Galerkin test function ω_i such that (18) holds, we can set

$$\gamma_i|_T = \omega_i|_T - \varphi_i|_T. \tag{30}$$

For example, for the formulations seen in the previous sections we have:

$$\begin{aligned}
\gamma_i^{F1}|_T &= \beta_i - \varphi_i|_T;\\
\gamma_i^{F2}|_T &= \delta_{\varphi_i} = \beta_i - \frac{1}{3};\\
\gamma_i^{F3/F4}|_T &= \chi_{C_i} - \varphi_i|_T.
\end{aligned} \tag{31}$$

4.2. Time-shifted stabilization operator

The second ingredient in our construction is the use of an explicit time-stepping scheme, combined with a shifted time discretization in the stabilization operator. We focus here on Runge–Kutta (RK) schemes, however other possibilities exist and will be explored in the future. Let us denote by $\delta u^k = u^k - u^n$ the increment of the kth step of a given explicit RK scheme. Similarly, let e^k be the kth step evolution operator so that for the problem

$$\frac{du}{dt} + e(u) = 0$$

we can rewrite each RK step as

$$\frac{\delta u^k}{\Delta t} + e^k = 0.$$

In particular, in the following we will denote by r^k the quantity

$$r^k = \frac{\delta u^k}{\Delta t} + e^k. \tag{32}$$

For example for the classical TVD RK2 scheme we have

$$\begin{cases} r^1 = \frac{\delta u^1}{\Delta t} + e^1 = 0, \quad e^1 = \vec{a}\cdot\nabla u^n, \\ r^2 = \frac{\delta u^2}{\Delta t} + e^2 = 0, \quad e^2 = \frac{1}{2}\vec{a}\cdot\nabla u^n + \frac{1}{2}\vec{a}\cdot\nabla u^1, \end{cases} \tag{33}$$

Similarly, the TVD RK3 scheme gives

$$\begin{cases} r^1 = \frac{\delta u^1}{\Delta t} + e^1 = 0, \quad e^1 = \vec{a}\cdot\nabla u^n, \\ r^2 = \frac{\delta u^2}{\Delta t} + e^2 = 0, \quad e^2 = \frac{1}{4}\vec{a}\cdot\nabla u^n + \frac{1}{4}\vec{a}\cdot\nabla u^1, \\ r^3 = \frac{\delta u^3}{\Delta t} + e^3 = 0, \quad e^3 = \frac{1}{6}\vec{a}\cdot\nabla u^n + \frac{1}{6}\vec{a}\cdot\nabla u^1 + \frac{2}{3}\vec{a}\cdot\nabla u^2. \end{cases} \tag{34}$$

With this notation we can write the kth step of the RK time integrator as

$$r^k = 0.$$

Its Galerkin discretization writes

$$\int_\Omega \varphi_i r^k(u_h)\,dx\,dy = \int_\Omega \varphi_i \frac{\delta u_h^k}{\Delta t}\,dx\,dy + \int_\Omega \varphi_i e^k(u_h)\,dx\,dy = 0.$$

The next step is to add the contribution of the bubble. The standard approach would be to write this contribution as

$$\sum_{T|i\in T}\int_T \gamma_i r^k(u_h)\,dx\,dy = \sum_{T|i\in T}\int_T \gamma_i\left(\frac{\delta u_h^k}{\Delta t} + e^k(u_h)\right)dx\,dy,$$

however, this would lead to a scheme in which the mass matrix depends on the bubble stabilization, which in turn might depend strongly on the unknown, eventually requiring the solution of a highly nonlinear algebraic system at each RK step. What we propose is to replace *only in the bubble contribution* the kth step residual $r^k(u_h)$ by a modified residual $\bar{r}^k(u_h)$, which makes use of a different approximation of the time derivative. In practice, we will look for $\bar{r}^k(u_h)$s differing from $r^k(u_h)$ only in the definition of the time increment, that is

$$\bar{r}^k(u_h) = \frac{\overline{\delta u^k}}{\Delta t} + e^k. \tag{35}$$

The constraints on $\bar{r}^k(u_h)$ guaranteeing that the overall accuracy of the discretization is not deteriorated will be discussed shortly. For the moment we observe that when adding this contribution we obtain with simple manipulations:

$$
\begin{aligned}
0 &= \int_\Omega \varphi_i r^k(u_h)dx\,dy + \sum_{T|i\in T}\int_T \gamma_i \bar{r}^k(u_h)dx\,dy \\
&= \int_\Omega \varphi_i \frac{\delta u_h^k}{\Delta t}dx\,dy + \int_\Omega \varphi_i\left(\overline{\frac{\delta u_h^k}{\Delta t}} + e^k(u_h)\right)dx\,dy + \sum_{T|i\in T}\int_T \gamma_i\left(\frac{\delta u_h^k}{\Delta t} + e^k(u_h)\right)dx\,dy - \int_\Omega \varphi_i \overline{\frac{\delta u_h^k}{\Delta t}}dx\,dy \\
&= \int_\Omega \varphi_i \frac{\delta u_h^k}{\Delta t} + \sum_{T|i\in T}\int_T (\varphi_i+\gamma_i)\left(\overline{\frac{\delta u_h^k}{\Delta t}} + e^k(u_h)\right)dx\,dy - \int_\Omega \varphi_i \overline{\frac{\delta u_h^k}{\Delta t}}dx\,dy = \int_\Omega \varphi_i \frac{\delta u_h^k}{\Delta t} + \sum_{T|i\in T}\Phi_i^{\mathrm{RK}(k)} - \int_\Omega \varphi_i \overline{\frac{\delta u_h^k}{\Delta t}}dx\,dy.
\end{aligned} \tag{36}
$$

The last relations are obtained by first adding and subtracting the Galerkin integral of the approximate time increment $\overline{\delta u^k}/\Delta t$, then using the properties of the bubble function γ_i (cf. equations (9) and (31)), and finally introducing the fully discrete split residuals:

$$
\Phi_i^{\mathrm{RK}(k)} = \int_T (\varphi_i+\gamma_i)\bar{r}^k(u_h)dx\,dy = \sum_{j\in T} m_{ij}\overline{\frac{\delta u_j^k}{\Delta t}} + \beta_i \phi^{\mathrm{RK}(k)}(u_h) \tag{37}
$$

with

$$
\phi^{\mathrm{RK}(k)} = \int_T f^k(u_h)dx\,dy \quad \text{and} \quad \sum_{j\in T}\Phi_j^{\mathrm{RK}(k)} = \int_T \bar{r}^h(u_h)dx\,dy = \Phi^{\mathrm{RK}(k)}. \tag{38}
$$

The final form of the scheme is

$$
\int_\Omega \varphi_i \frac{\delta u_h^k}{\Delta t}dx\,dy - \int_\Omega \varphi_i \overline{\frac{\delta u_h^k}{\Delta t}}dx\,dy = -\sum_{T|i\in T}\Phi_i^{\mathrm{RK}(k)}, \tag{39}
$$

where now the mass matrix obtained from the first integral is independent on the solution.

All that remains to do is to derive a sufficient condition on the $\bar{r}^k$ guaranteeing that the accuracy of the Runge–Kutta Galerkin approximation is not lost when adding the bubble contribution. To do this we use a truncation error analysis, following the approach of [31]. All the details of the analysis are given in two appendices at the end of the paper. The general idea of the proof is, given a sufficiently smooth classical solution w, and a smooth function $\psi \in C_0^1(\Omega)$, to verify under which conditions the truncation error

$$
\mathcal{E}_n = \left|\sum_{i\in\mathcal{T}_h}\psi_i\int_\Omega \varphi_i\left(\frac{\delta w_h^{n+1}}{\Delta t} + e^{n+1}(w_h)\right)dx\,dy + \sum_{i\in\mathcal{T}_h}\psi_i\sum_{T|i\in T}\int_T \gamma_i\left(\overline{\frac{\delta w_h^{n+1}}{\Delta t}} + e^{n+1}(w_h)\right)dx\,dy\right| \tag{40}
$$

is of an order $\mathcal{O}(h^p)$. The analysis reported in Appendix A and B is done for the general case $p \geqslant 2$, even though the paper focuses only on the case $p = 2$. Note that in the definition of the error we have used the notation introduced in the previous section. This means that $e^{n+1}(w_h)$ represents the discrete evolution operator of the last RK step, which actually makes use of flux values at *known* time-steps (cf. equations (33) and (34)). The analysis makes use of the following two hypotheses.

Hypothesis 4.1 (*RK truncation error*). Given a smooth classical solution w such that $\partial_t w + \nabla\cdot\mathcal{F}(w) = 0$, a pth order RK scheme verifies the truncation error estimate

$$
r^{n+1}(w) = \frac{\delta w^{n+1}}{\Delta t} + e^{n+1}(w) = C_{\mathrm{RK}}\Delta t^p.
$$

Hypothesis 4.2 (*Semi-discrete approximate residual estimate*). Given a smooth classical solution w such that $\partial_t w + \nabla\cdot\mathcal{F}(w) = 0$, the approximate semi-discrete residual $\bar{r}$ verifies the estimate

$$
\bar{r}^{n+1}(w) = \overline{\frac{\delta w^{n+1}}{\Delta t}} + e^{n+1}(w) = \overline{C}_{\mathrm{RK}}\Delta t^l
$$

for some $l \leqslant p$.

The main result is summarized by the following proposition.

Proposition 4.3 (Accuracy and time-stepping). *Given a pth order spatial approximation and a pth order RK scheme verifying Hypothesis 4.1, the truncation error (40) verifies an estimate of the type*

$$
\mathcal{E}_n \leqslant Ch^p
$$

provided that

1. *The bubble γ_i is uniformly bounded.*
2. The approximate semi-discrete residual verifies Hypothesis 4.2 with

$$l \geqslant p-1.$$

In particular, in the second order case of interest here, it is enough to provide definitions of the approximate time increments yielding a first order semi-discrete operator.

Remark 4.4 (*Accuracy, time-stepping, and distribution coefficients*). As seen in Section 3, for all the known consistent formulations of RD we can provide define the bubble function as $\gamma_i = \omega_i - \psi_i$ is always bounded. For the formulations recalled in Section 3, ω_i, and hence γ_i, is bounded whenever the distribution coefficients β_i are.

To end the construction we give particular definitions of $\bar{r}^k$ that satisfy Hypothesis 4.2 (see Appendix B):

RK2 scheme

$$\begin{aligned}
&\overline{\delta u^1} = 0 \Rightarrow \bar{r}^1 = \nabla\cdot\boldsymbol{\mathcal{F}}(u^n),\\
&\overline{\delta u^2} = \overline{\delta u^{n+1}} = u^1 - u^n \Rightarrow \bar{r}^2 = \frac{u^1-u^n}{\Delta t} + \frac{\nabla\cdot\boldsymbol{\mathcal{F}}(u^n)+\nabla\cdot\boldsymbol{\mathcal{F}}(u^1)}{2}.
\end{aligned} \tag{41}$$

RK3 scheme

$$\begin{aligned}
&\delta\bar{u}^1 = 0 \Rightarrow \bar{r}^1 = \nabla\cdot\boldsymbol{\mathcal{F}}(u^n),\\
&\delta\bar{u}^2 = \frac{u^1-u^n}{2} \Rightarrow \bar{r}^2 = \frac{u^1-u^n}{2\Delta t} + \frac{\nabla\cdot\boldsymbol{\mathcal{F}}(u^n)+\nabla\cdot\boldsymbol{\mathcal{F}}(u^1)}{2},\\
&\delta\bar{u}^3 = \delta\bar{u}^{n+1} = 2(u^2-u^n) \Rightarrow \bar{r}^3 = \frac{2(u^2-u^n)}{\Delta t} + \frac{\nabla\cdot\boldsymbol{\mathcal{F}}(u^n)+\nabla\cdot\boldsymbol{\mathcal{F}}(u^1)+4\nabla\cdot\boldsymbol{\mathcal{F}}(u^2)}{6}.
\end{aligned} \tag{42}$$

Note that in this case the coefficients involved in the definition take into account the fact that u^1 and u^2 are initial guesses for the solution at times $t^n + \Delta t$ and $t_n + \Delta t/2$, respectively.

4.3. High order mass lumping

Scheme (39) still requires the inversion of the Galerkin mass matrix at each RK step. Even though this matrix is constant and symmetric positive definite, its inversion does introduce an additional unnecessary computational cost.

So, the last step in our construction is the introduction of a high order mass lumping strategy. High order mass lumping for Galerkin discretizations of the wave equation are developed *e.g.* in [23,39,38]. We refer to these articles, and to the references therein, for details on the construction. Here we just recall its basic principles, and specialize it to the simple P^1 case of interest in our case.

The basic idea is to replace the Galerkin integral of the time derivative by its approximation obtained by means of a quadrature rule:

$$\int_T \varphi_i \partial_t \nabla u_h dx\,dy \approx \sum_{x_q} |T|\omega_q \varphi_i(x_q)\partial_t u_h(x_q).$$

It can be shown that *a sufficient condition for this approximation to keep a truncation error of $\mathcal{O}(h^p)$ is for the quadrature formula to integrate exactly polynomials of degree $p-1$* [23,39,38].

The interesting application of this approach is when *the quadrature points coincide with all the degrees of freedom of the element*. In this case, one ends with

$$\int_T \varphi_i \partial_t \nabla u_h dx\,dy \approx \sum_{j\in T} |T|\omega_j \varphi_i(x_j)\partial_t u_j = \omega_i |T|\partial_t u_j$$

since $\varphi_i(x_j) = \delta_{ij}$. So to apply high order mass lumping, retaining a truncation error of $\mathcal{O}(h^p)$, *the finite element space has to be such that the degrees of freedom define on each element a quadrature formula integrating exactly polynomials of degree $p-1$*. Examples of such spaces can be found in [23,39,38]. In the P^1 case we are very lucky since the formula

$$\int_T g(x,y)dx\,dy \approx \sum_{j\in T} \frac{1}{3}|T| g_j$$

does integrate exactly linear polynomials, hence it guarantees the preservation of a $\mathcal{O}(h^2)$ truncation error. In particular, we obtain for the mass matrix the well known result:

$$\int_\Omega \varphi_i \partial_t u_h\,dx\,dy \approx \sum_{T\in|i\in T} \frac{|T|}{3}\partial_t u_i = |S_i|\partial_t u_i$$

with

$$|S_i| = \sum_{T|i\in T} \frac{1}{3}|T|. \tag{43}$$

Before concluding with the final construction of our schemes we note that in the P^1 case, a different interpretation is obtained by using (22). In particular, if we take $K = 3$ and apply the mass matrix modification to the Galerkin scheme we get:

$$\bar{m}_{ij} = \overbrace{\frac{|T|}{12}(\delta_{ij}+1)}^{\text{Galerkin}} + \overbrace{\frac{|T|}{12}(3\delta_{ij}-1)}^{3\delta m_{ij}} = \frac{|T|}{3}\delta_{ij}.$$

Which again shows that mass lumping for the Galerkin scheme does not reduce the asymptotic accuracy in the P^1 case, however it does introduce a degree of dissipation.

4.4. Fully explicit schemes

We now put together all the ingredients presented so far to obtain the final discretization. Two possibilities exist, leading to two distinct classes of methods.

4.4.1. Selectively lumped (SL) schemes

If in the last line of (36) only the mass-matrix corresponding to the first Galerkin integral is lumped we obtain the following *selectively lumped* explicit formulation:

$$|S_i|\frac{\delta u_i^k}{\Delta t} = -\sum_{T|i\in T}\left(\Phi_i^{\mathrm{RK}(k)} - \int_T \varphi_i \frac{\overline{\delta u_h^k}}{\Delta t}\,dx\,dy\right). \tag{44}$$

In this case, the effect of the lumping leads to the following modification of the RD mass matrix:

$$m_{ij}^{\mathrm{SL}} = m_{ij}^T - m_{ij}^G, \quad m_{ij}^G = \frac{|T|}{12}(\delta_{ij}+1) \tag{45}$$

with m_{ij}^G the Galerkin mass matrix.

4.4.2. Globally lumped (GL) schemes

When lumping both Galerkin mass matrices we obtain the following *globally lumped* explicit formulation:

$$|S_i|\frac{\delta u_i^k - \overline{\delta u_i^k}}{\Delta t} = -\sum_{T|i\in T}\Phi_i^{\mathrm{RK}(k)}. \tag{46}$$

In this case, there is no modification on the residual distribution mass matrix, however, the lumping modifies the explicit iterations that now depend on the definition of $\overline{\delta u^k}$.

When combining this definition with the explicit RK2 scheme with shifted time operator in the stabilization (cf. equations (33) and (41)), we obtain for the SL schemes

$$\begin{cases} |S_i|\frac{u_i^1-u_i^n}{\Delta t} = -\sum_{T|i\in T}\beta_i\phi(u_h^n), \\ |S_i|\frac{u_i^{n+1}-u_i^n}{\Delta t} = -\sum_{T|i\in T}\left(\Phi_i^{\mathrm{RK2}(2)} - \sum_{j\in T} m_{ij}^G\frac{u_j^1-u_j^n}{\Delta t}\right) \end{cases} \tag{47}$$

with m_{ij}^G as in (45), and with

$$\Phi_i^{\mathrm{RK2}(2)} = \sum_{j\in T} m_{ij}^T\frac{u_j^1-u_j^n}{\Delta t} + \frac{1}{2}\beta_i\left(\phi(u_h^n)+\phi(u_h^1)\right).$$

The update for the GL schemes is somewhat simpler and given by

$$\begin{cases} |S_i|\frac{u_i^1-u_i^n}{\Delta t} = -\sum_{T|i\in T}\beta_i\phi(u_h^n), \\ |S_i|\frac{u_i^{n+1}-u_i^1}{\Delta t} = -\sum_{T|i\in T}\Phi_i^{\mathrm{RK2}(2)}. \end{cases} \tag{48}$$

Conversely, in the RK3 case we get for the SL schemes (cf. equations (34) and (42))

$$\begin{cases} |S_i|\frac{u_i^1-u_i^n}{\Delta t} = -\sum\limits_{T|i\in T}\beta_i\phi(u_h^n), \\ |S_i|\frac{u_i^2-u_i^n}{\Delta t} = -\sum\limits_{T|i\in T}\left(\Phi_i^{\mathrm{RK3}(2)} - \sum\limits_{j\in T} m_{ij}^G \frac{u_j^1-u_j^n}{2\Delta t}\right), \\ |S_i|\frac{u_i^{n+1}-u_i^n}{\Delta t} = -\sum\limits_{T|i\in T}\left(\Phi_i^{\mathrm{RK3}(3)} - \sum\limits_{j\in T} m_{ij}^G 2\frac{u_j^2-u_j^n}{\Delta t}\right) \end{cases} \tag{49}$$

with m_{ij}^G as in (45), and with

$$\Phi_i^{\mathrm{RK3}(2)} = \sum_{j\in T} m_{ij}^T \frac{u_j^1-u_j^n}{2\Delta t} + \frac{1}{4}\beta_i\left(\phi(u_h^n)+\phi(u_h^1)\right)$$

and

$$\Phi_i^{\mathrm{RK3}(3)} = \sum_{j\in T} m_{ij}^T 2\frac{u_j^2-u_j^n}{\Delta t} + \beta_i\left(\frac{1}{6}\phi(u_h^n)+\frac{1}{6}\phi(u_h^1)+\frac{2}{3}\phi(u_h^2)\right).$$

As before, the update for the globally lumped schemes is somewhat simpler and given by

$$\begin{cases} |S_i|\frac{u_i^1-u_i^n}{\Delta t} = -\sum\limits_{T|i\in T}\beta_i\phi(u_h^n), \\ \frac{|S_i|}{\Delta t}\left(u_i^2 - \frac{u_i^1+u_i^n}{2}\right) = -\sum\limits_{T|i\in T}\Phi_i^{\mathrm{RK3}(2)}, \\ \frac{2|S_i|}{\Delta t}\left(\frac{u_i^{n+1}+u_i^n}{2} - u_i^2\right) = -\sum\limits_{T|i\in T}\Phi_i^{\mathrm{RK3}(3)}, \end{cases} \tag{50}$$

Remark 4.5 (*Fluctuations/signals*). Both formulations, the one based on selective lumping and the one based on global lumping, allow to see the RD component of the discretization as an error between two different approximations of the unknown at certain time levels. When using the formulation F1 of the RD discretization (cf. Section 3, equation (13)), the second step of the RK2 scheme with selective lumping can be recast as

$$|S_i|\frac{u_i^{n+1}-u_i^n}{\Delta t} - \int_\Omega \varphi_i \frac{u_h^1-u_h^n}{\Delta t} = -\sum_{T|i\in T}\beta_i\Phi^{\mathrm{RK2}(2)}, \tag{51}$$

where

$$\Phi^{\mathrm{RK2}(2)} = \int_T \left(\frac{u_h^1-u_h^n}{\Delta t} + \frac{1}{2}\nabla\cdot\mathcal{F}_h(u_h^n) + \frac{1}{2}\nabla\cdot\mathcal{F}_h(u_h^1)\right)dx\,dy.$$

Clearly equation (51) expresses the error between two local approximations of the time variation of the unknown as a function of signals proportional to elemental errors represented by the residual $\Phi^{\mathrm{RK2}(2)}$. This is even more apparent in the case of the globally lumped scheme which reads, in RK2 case:

$$|S_i|\frac{u_i^{n+1}-u_i^1}{\Delta t} = -\sum_{T|i\in T}\beta_i\Phi^{\mathrm{RK2}(2)}. \tag{52}$$

The RK3 version of the last equation is obtained immediately from equation (50). In (55) the RD weighted average on the right-hand side expresses the error between two different approximations of the unknown at time t^{n+1}. The same remarks applies of course to the case of the RK3 schemes. In some way the explicit formulations proposed here lead us back to the original ideas of Roe [34] in which the nodal error is proportional to the signals sent by surrounding elements.

Remark 4.6 (*Relations with explicit predictor–corrector*). The explicit formulation proposed here is also related to the explicit predictor/multi-corrector formulation of the SUPG scheme used for example in [24–26] (see also [40,28,36]). In the simplest setting, in this formulation on replaces an implicit time integrator by a finite number of explicit steps. In the case of the Crank–Nicholson time integrator for example the idea is to rewrite the SUPG scheme as

$$|S_i|\frac{u_i^1-u_i^n}{\Delta t} = -\int_\Omega \varphi_i\vec{a}\cdot\nabla u_h^n dx\,dy + \sum_{T|i\in T}\int_T \vec{a}\cdot\nabla\varphi_i\tau\vec{a}\cdot\nabla u_h^n dx\,dy,$$

$$|S_i|\frac{u_i^k-u_i^n}{\Delta t} = -\int_\Omega \varphi_i\vec{a}\cdot\nabla\frac{u_h^{k-1}+u_h^n}{2}dx\,dy + \sum_{T|i\in T}\int_T \vec{a}\cdot\nabla\varphi_i\tau\left(\frac{u_h^{k-1}-u_h^n}{\Delta t} + \vec{a}\cdot\nabla\frac{u_h^{k-1}+u_h^n}{2}\right)dx\,dy,$$

where $k \geqslant 2$ and $u_i^{n+1} = u_i^{k_{\max}}$. The second relation can immediately be recast as

$$|S_i|\frac{u_i^k-u_i^n}{\Delta t}=-\sum_{T|i\in T}\left(\sum_{T|i\in T}\Phi_i^{\mathrm{SUPG}(k)}-\int_T\varphi_i\frac{u_h^{k-1}-u_h^n}{\Delta t}dxdy\right)$$

with

$$\Phi_i^{\mathrm{SUPG}(k)}=\int_T(\varphi_i+\vec{a}\cdot\nabla\varphi_i\tau)\left(\frac{u_h^{k-1}-u_h^n}{\Delta t}+\vec{a}\cdot\nabla\frac{u_h^{k-1}+u_h^n}{2}\right)dxdy$$

and

$$\sum_{j\in T}\Phi_j^{\mathrm{SUPG}(k)}=\Phi^k=\int_T\left(\frac{u_h^{k-1}-u_h^n}{\Delta t}+\vec{a}\cdot\nabla\frac{u_h^{k-1}+u_h^n}{2}\right)dxdy.$$

This is basically the selectively lumped formulation of the SUPG scheme in RD form. In particular, when using only one correction step we end up exactly with the RK2 scheme (47).

Remark 4.7 (*Explicit residual-based finite volume formulation*). The approach presented here finds application also in the case of finite volume discretizations where the stabilization operator is proportional to some local approximation of the residual, rather than to local variations of the solution. Such schemes have been proposed for example in [14,11] and, in a different spirit, in [12]. The schemes of [14,11] in their basic formulation can be rewritten as

$$|C_i|\frac{du_i}{dt}+\oint_{\partial C_i}\mathcal{H}_C\cdot\hat{n}dl-\frac{1}{2}\sum_j h_j\Psi_{ij}\Phi_{ij}=0, \tag{53}$$

where $\mathcal{H}_C$ is a centered finite volume numerical flux, while the last term represent stabilization terms. These terms are function of a local residual Φ_{ij}, computed on the staggered cell C_{ij} (cf. Fig. 2) and defined as [14,11]

$$\Phi_{ij}=\int_{C_{ij}}\left(\frac{du_h}{dt}+\nabla\cdot\mathcal{F}_h(u_h)\right)dxdy,$$

where now u_h is a polynomial approximation of the unknown *reconstructed starting from cell averages*. We refer to [14,11] for further details, and in particular for the definition of the local mesh size h_j, and of the Ψ_{ij} parameter in (53). The important point is that the residual Φ_{ij} has to include the time derivative of the numerical unknown to attain consistency in the spatial discretization. In [14,11] the authors use the same discrete operator to approximate both the time derivative of u_i in (53), and in Φ_{ij}. this naturally leads to the appearance of a mass matrix rendering the scheme implicit *in space*. The approach proposed here allows to overcome this limitation allowing the construction of an explicit RK schemes in which the time derivative in Φ_{ij} is approximated by time increments using known values of the discrete solution. In the RK2 case for example the scheme would read:

$$|C_i|\frac{u_i^1-u_i^n}{\Delta t}+\oint_{\partial C_i}\mathcal{H}_C^n\cdot\hat{n}dl-\frac{1}{2}\sum_j h_j\Psi_{ij}\int_{C_{ij}}\nabla\cdot\mathcal{F}_h^n dxdy=0,$$

$$|C_i|\frac{u_i^{n+1}-u_i^n}{\Delta t}+\oint_{\partial C_i}\frac{\mathcal{H}_C^n+\mathcal{H}_C^1}{2}\cdot\hat{n}dl-\frac{1}{2}\sum_j h_j\Psi_{ij}\int_{C_{ij}}\left(\frac{u_h^1-u_h^n}{\Delta t}+\frac{\nabla\cdot\mathcal{F}_h^n+\nabla\cdot\mathcal{F}_h^1}{2}\right)dxdy=0$$

with $\mathcal{H}_C^1=\mathcal{H}_C(u_h^1)$ and $\mathcal{F}_h^1=\mathcal{F}_h(u_h^1)$.

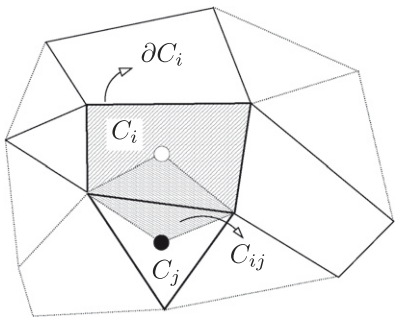

Fig. 2. Residual based finite volume. Cells C_i and C_j, and staggered cell C_{ij}.

5. Schemes used in the numerical experiments

This section is devoted to the description of the schemes actually used in the numerical tests discussed in the following paragraphs, and of some details relative to their implementation. We will discuss the results obtained with four well known schemes: the LDA scheme, the blended LDAN scheme or B scheme, the Streamline Upwind scheme, or SU scheme for short, and a centered Blended scheme, Bc for short, constructed starting from the limited stabilized Lax-Friedrich's scheme of [2]. The results obtained with other RD schemes are very similar in nature. An important remark is that *so far we still have not worked on the adaptation of nonlinear RD discretizations to the construction proposed in the paper*. This means that we limited ourselves to code the schemes as they are presented in the literature. Improvements will be made in the future concerning strict preservation of positivity. Even so, as we will see, the numerical results are excellent, and confirm our theoretical analysis.

5.1. LDA scheme

We test our construction on the well known second order linear multidimensional upwind LDA scheme, defined by the distribution coefficients [18]:

$$\beta_i^{\mathrm{LDA}} = k_i^+ \left(\sum_{j \in T} k_j^+ \right)^{-1}, \tag{54}$$

where, using the notation of equation (2), we define $\forall T \in \mathcal{T}_h$

$$k_i = \frac{1}{2} \frac{\partial \boldsymbol{\mathcal{F}}(\bar{u})}{\partial u} \cdot \vec{n}_i \tag{55}$$

with $\bar{u}$ the arithmetic average of the values of u_h in the nodes of T. Note that in the case of a system of conservation laws, the k_is are matrices, and their sign in (54) is computed in the standard matrix sense, via eigenvalue decomposition. For more details on the definition and properties of the LDA scheme, the reader is referred to [18,1].

In the scalar case we will compare the results obtained when using the different formulations recalled in Section 3. In particular, the scheme has been coded exactly as described in equations (47) and (49), for the selectively lumped scheme, and in equations (48) and (50) for the global lumped scheme. In both cases, we replace the quantities $\Phi_i^{\mathrm{RK2}(k)}$ and $\Phi_i^{\mathrm{RK3}(k)}$ by (see equations (38), (41), and (42) for the notation)

$$\Phi_i^{\mathrm{LDA}(k)} = \sum_{j \in T} m_{ij}^{\mathrm{LDA}} \overline{\delta u_j^k} + \Delta t \beta_i^{LDA} \phi^{\mathrm{RK}(k)}. \tag{56}$$

In particular, the form of the mass matrix m_{ij}^{LDA} will depend of the formulation chosen (cf. Section 3). To shorten the text we will lump together the acronyms when referring to a scheme. For example, we shall speak of the LDA-F1-SL-RK2 when referring to the scheme obtained using the LDA distribution coefficients, the mass matrix of the formulation 1, selective lumping, and the RK2 scheme in time. Similarly for all the other combinations.

5.2. Blended LDA-N scheme

As suggested by its name, the Blended LDA-N scheme, or B scheme for short, is a blending between the LDA scheme of Section 5.1 with the first order positive multidimensional upwind N scheme defined by the spatial splitting [18,1,16]

$$\phi_i^{\mathrm{N}} = k_i^+ (u_i - u_{\mathrm{in}}), \quad u_{\mathrm{in}} = \left(\sum_{j \in T} k_j^+ \right)^{-1} \left(-\phi(u_h) + \sum_{j \in T} k_j^+ u_j \right).$$

In particular, following [4], we set for the B scheme

$$\Phi_i^{\mathrm{B}(k)} = (1 - l(u_h)) \Phi_i^{\mathrm{LDA}(k)} + l(u_h) \Phi^{\mathrm{N}(k)} \tag{57}$$

with $\Phi_i^{\mathrm{LDA}(k)}$ given by (56) and with

$$\Phi_i^{\mathrm{N}(k)} = \frac{|T|}{3} \overline{\delta u_i^k} + \Delta t \phi_i^{\mathrm{N}(k)}$$

having denoted by $\phi_i^{\mathrm{N}(k)}$ the spatial contribution of the N scheme corresponding to the kth RK step. Expression (57) is used in (47)–(50) to replace $\Phi_i^{\mathrm{RK2}(k)}$ and $\Phi_i^{\mathrm{RK3}(k)}$.

Concerning the blending parameter $l(u_h)$ we have used the standard definition of Deconinck et al. [19,16] (cf. also equation (38)):

$$l(u_h) = \frac{|\Phi^{\mathrm{RK}(k)}|}{\sum_{j \in T} |\Phi_j^{\mathrm{N}(k)}|}$$

for systems of equations, the blending procedure has been performed on residuals projected in characteristic directions, as explained in [5,4].

As a last remark, we note that only when using global lumping for $l(u_h) = 1$ does the B scheme defined by (57) reduce to the N scheme with RK time integration. In the selective lumping case, for $l(u_h) = 1$ we get (cf. equation (44)

$$|S_i|\frac{\delta u_i^k}{\Delta t} + \sum_{T|i\in T}\phi_i^{N(k)} = |S_i|\frac{\overline{\delta u_i^k}}{\Delta t} - \int_\Omega \varphi_i \frac{\overline{\delta u_h^k}}{\Delta t}\,dx\,dy,$$

where the left hand side corresponds to the kth RK step of the N scheme, while the right hand side contains some kind of anti-diffusive correction (cf. Section 3.).

5.3. The SU scheme

To test the behavior of our formulation with different type of discretizations, we also consider centered schemes. The first is referred to in the RD literature either as SUPG scheme or as LW scheme. It is defined by the distribution coefficients

$$\beta_i^{SU} = \frac{1}{3} + k_i\tau. \tag{58}$$

Independently on the definition of the scaling parameter τ, the second term on the last definition introduces some Streamline Upwinding in the distribution [18], which is why we refer to this scheme as to the SU scheme. In our computations we have taken

$$\tau = \left(\sum_{j\in T}|k_j|\right)^{-1}. \tag{59}$$

For the Euler equations, last expression is meant in the usual matrix sense.

Finally, we replace the quantities $\Phi_i^{RK2(k)}$ and $\Phi_i^{RK3(k)}$ by (see equations (38), (41) and (42) for the notation)

$$\Phi_i^{SU(k)} = \sum_{j\in T} m_{ij}^{SU}\overline{\delta u_j^k} + \Delta t\beta_i^{SU}\phi^{RK(k)}. \tag{60}$$

As for the LDA scheme, also for the SU scheme the form of the mass matrix m_{ij}^{SU} depends of the formulation chosen (cf. Section 3).

5.4. Central blended scheme

In [2,32] the authors introduce a centered discretization based on a nonlinear variant of a Lax-Friedrich's scheme. This limited stabilized Lax-Friedrich's scheme, or LLFs scheme, is obtained starting from the positive first order Lax-Friedrich's (LF) splitting

$$\phi_i^{LF} = \frac{1}{3}\left(\phi(u_h) + \alpha_{LF}\sum_{j\in T}(u_i - u_j)\right), \tag{61}$$

where α_{LF} is the Lax-Friedrich's dissipation coefficient which we set to

$$\alpha_{LF} = \frac{1}{2}a_T h_T, \quad a_T = \max_{j|\in T}\left\|\frac{\partial \mathcal{F}(u_j)}{\partial u}\right\|$$

in the scalar case, while for the Euler equations we have set

$$\alpha_{LF} = \frac{1}{2}\max_{j|\in T}(\|\vec{u}_j\| + a_j)h_T$$

with $\vec{u}$ the flow speed, a the speed of sound, and h_T a reference length for element T.

The LF scheme is only first order. To obtain a formally second order nonlinear splitting we proceed as follows. First we define the LF–RK splitting

$$\Phi_i^{LF(k)} = \frac{|T|}{3}\overline{\delta u_i^k} + \Delta t\phi_i^{LF(k)}$$

having denoted by $\phi_i^{LF(k)}$ the kth RK step of the spatial operator (61). Next, we compute bounded distribution coefficients by applying a sign preserving nonlinear mapping. Several ways of doing this exist, and we refer to [6,2] for a discussion. Here, we set:

$$\beta_i^{\mathrm{LLF}} = \frac{\max\left(0, \Phi_i^{\mathrm{LF}(k)}\Phi^{\mathrm{RK}(k)}\right)}{\sum_{j\in T}\max\left(0, \Phi_j^{\mathrm{LF}(k)}\Phi^{\mathrm{RK}(k)}\right)}. \tag{62}$$

The limited LF scheme is then defined by

$$\Phi_i^{\mathrm{LLF}(k)} = \beta_i^{\mathrm{LLF}}\Phi^{\mathrm{RK}(k)}.$$

As shown in previous work [2,32,30], the limiter (62) not taking into account the directional propagation of the information typical of hyperbolic problems, the LLF scheme shows mild spurious modes that eventually reduce its accuracy to first order. This is cured as in the above references by adding an upwind bias inspired by the SU scheme:

$$\beta_i^{\mathrm{LLFs}} = \beta_i^{\mathrm{LLF}} + \delta(u_h)k_i\tau \tag{63}$$

with τ as in (59). We refer the reader to [2,32,30] for more details on the theoretical background leading to this choice. We limit ourselves to recall that $\delta(u_h)$ is a smoothness sensor such that $\delta(u_h) = 1$ in smooth areas, while $\delta = \mathcal{O}(h_T)$ in presence of discontinuities. In our computations we have set in the scalar case [2,32,30]

$$\delta(u_h) = \min\left(1, \frac{\Delta t h_T^2 a_T |u|_T}{|\Phi^{\mathrm{RK}(k)}|}\right), \tag{64}$$

where $|u|_T$ is the maximum of the absolute value of the solution over the element. For the Euler equations, the extension is done following [2]: the limiter (62) is evaluated on residual projected on local characteristic directions, while the $|\Phi^{\mathrm{RK}(k)}|$ in (64) is replaced by the *scalar* entropy component of $\Phi^{\mathrm{RK}(k)}$. This is computed as

$$\varphi_s = l_0 \cdot \Phi^{\mathrm{RK}(k)},$$

where l_0 is the left eigenvector of the flux Jacobian corresponding to the entropy wave. For the Euler equations $\delta(u_h)$ is then the scalar quantity (see [2] for more)

$$\delta(u_h) = \min\left(1, \frac{\Delta t h_T^2}{|\varphi_s|}\right). \tag{65}$$

Normally, we would set

$$\Phi_i^{\mathrm{LLFs}(k)} = \beta_i^{\mathrm{LLFs}}\Phi^{\mathrm{RK}(k)} \tag{66}$$

and replace $\Phi_i^{\mathrm{RK2}(k)}$ and $\Phi_i^{\mathrm{RK3}(k)}$ in (47)–(50) by (66). However, we found that much better results are obtained, at negligible extra cost, by using the central blended scheme, or Bc scheme for short, defined by

$$\Phi_i^{\mathrm{Bc}(k)} = \beta_i^{\mathrm{Bc}}\Phi^{\mathrm{RK}(k)}, \quad \beta_i^{\mathrm{Bc}} = \delta(u_h)\beta_i^{\mathrm{SU}} + (1-\delta(u_h))\beta_i^{\mathrm{LLF}} \tag{67}$$

From definition (65) we see that being $\delta(u_h)$ a scalar quantity, the extra cost with respect to the LLFs scheme is negligible.

5.5. Computation of the time step

All the numerical results presented in the following section have been obtained by computing the time step as (cf. Section 5.3):

$$\Delta t = \min_{i\in T_h}\frac{|S_i|}{\sum_{T|i\in T}\alpha_{\mathrm{LF}}}. \tag{68}$$

For all the nonlinear problems considered, α_{LF} is evaluated using solution values at the last known time step.

A Fourier analysis on structured triangulations is under way to have a better estimate of the time step stability limit for the linear schemes.

6. Scalar results

The scalar tests we present have two objectives: verify the accuracy of our explicit formulation for different forms of the mass matrix, and for schemes of different nature (multidimensional upwind, and centered); test the non-oscillatory nature of the results obtained with the nonlinear schemes, when no modifications are introduced to take into account the additional terms introduced by RK formulation.

Unless stated, all the numerical tests, including the Euler tests, have been performed on unstructured triangulations with the topology shown on Fig. 3.

6.1. Advection of a smooth profile: grid convergence

The first test involves the simple scalar equation

$$\partial_t u + \partial_x u = 0$$

solved on the rectangular domain $[0,2] \times [0,1]$. The initial solution is set to

$$u_0 = \begin{cases} \cos^2(2\pi r) & \text{if } r \leqslant 0.25 \\ 0 & \text{otherwise} \end{cases}$$

with $r^2 = (x-0.5)^2 + (y-0.5)^2$. We solve the problem up to time $t = 1$ on a series of five meshes with the topology shown on Fig. 3. The coarsest mesh has a reference element size $h \approx 1/20$ (10 points in the smooth cosinusoidal profile). The other meshes are obtained via four steps of conformal refinement. We use this test to study the accuracy of the different schemes discussed in the paper. The accuracy is monitored by the convergence of the L^1 norm of the error with respect to the exact solution. The behavior of the L^∞ and L^2 norms is qualitatively and quantitatively very similar.

The first exercise is to verify that indeed our RK formulation leads to second order discretizations, independently on the starting form of the (consistent) mass matrix. We perform the test for all the mass matrix formulations for the LDA scheme, which is the most popular multidimensional upwind RD scheme.

The results are summarized in Figs. 4 and 5, where we report the grid convergence history and the rate of convergence history, respectively. The first remark we can make is that our explicit formulation does lead to a second order discretization. This is clear especially from the rates of convergence observed. What is more interesting is that the RK2 schemes all yield the same accuracy, while the RK3 scheme with global lumping seem to actually be less and less accurate as the mesh is refined. We believe this might be the consequence of a (mild) linear stability problem. We are currently performing a Fourier analysis on structured grids to better understand this behavior. There are minor differences between the different mass matrix forms which, in our opinion, do not justify the use of the more complex formulations F3 and F4 (cf. Section 3), especially in view of the extension to systems.

We repeat the same exercise with the SU scheme, only this time we only test the mass matrix formulations F1 and F2 (cf. Section 3). The results are shown on Fig. 6. The same remarks made for the LDA scheme apply also to the SU distribution: second order of accuracy is obtained already with the RK2 scheme, independently of the mass matrix and lumping choices; the RK3 scheme with global lumping suffers from a drop in the convergence rate, which might be caused by the presence of a linear instability.

We now come to the nonlinear schemes. We first test the B scheme, using either formulation F1, or formulation F2 for the LDA mass matrix. The results are displayed on Fig. 7. The asymptotic rate of convergence obtained is about 1.75–1.8, independently on the formulation. Clearly, when using global lumping, the drop in convergence speed of the LDA affects the B scheme as well. Lastly, on Fig. 8 we report the results obtained with the Bc scheme. Once more, we observe asymptotic convergence rates ranging from 1.7 to 1.9, with the exception of the RK3 scheme in conjunction with global lumping.

We believe these tests confirm our theoretical construction. In particular the fact that with the RK2 scheme one already obtains a second order discretization. Moreover, the fact that different forms of the mass matrix lead to very similar accuracy properties leads us to the conclusion that the choice of the form of the mass matrix should be done on the basis of stability (or positivity eventually) considerations. This is the objective of our current investigations.

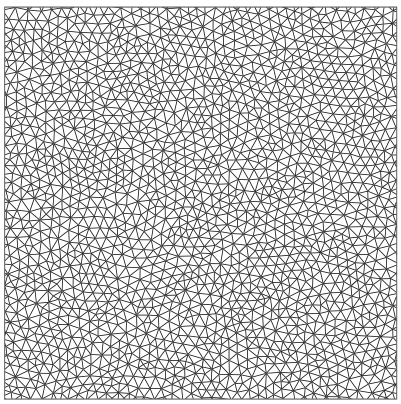

Fig. 3. Typical topology of the meshes used in the numerical tests.

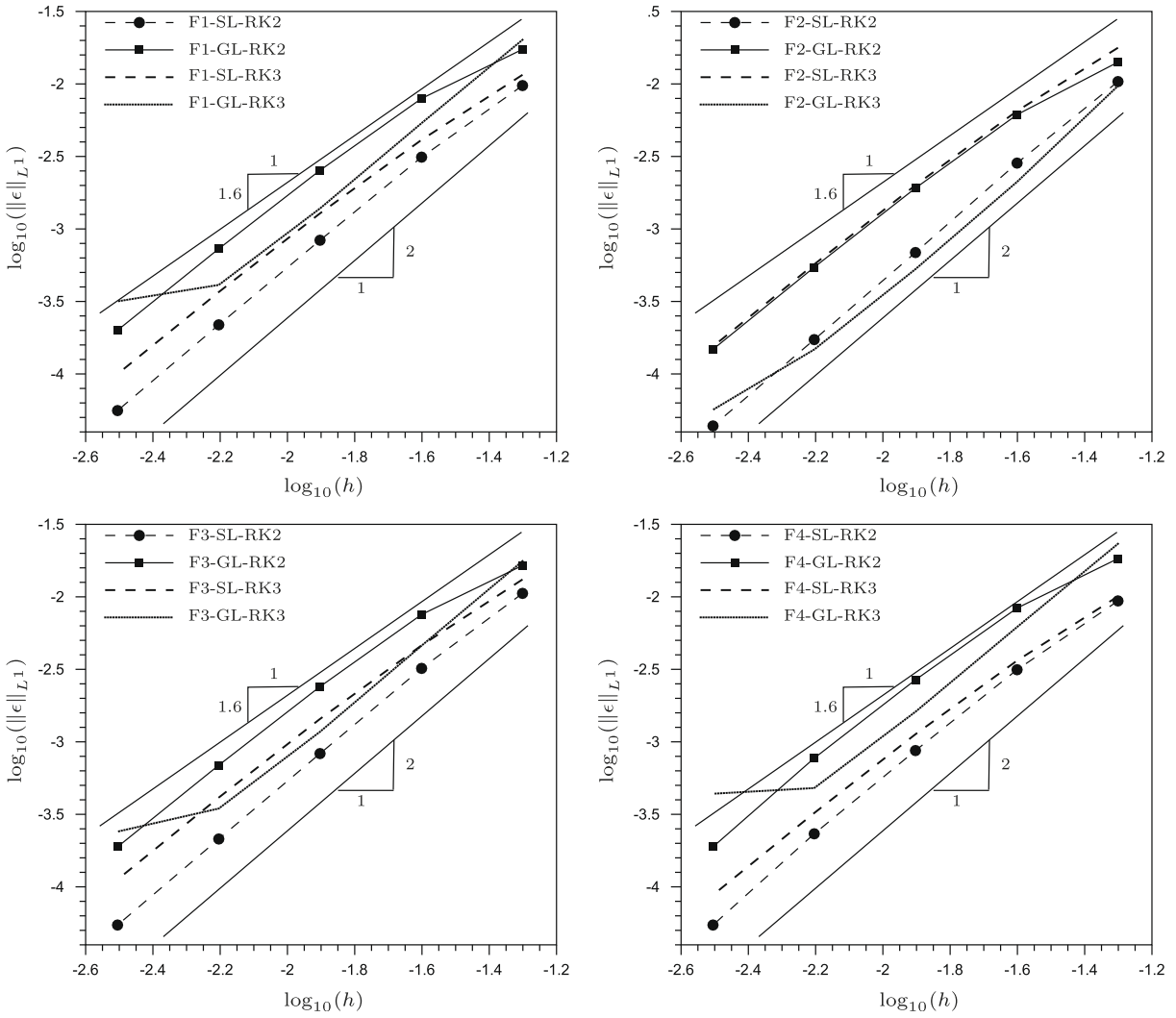

Fig. 4. Scalar advection: grid convergence for the LDA scheme. Top-left: formulation F1. Top-right: formulation F2. Bottom-left: formulation F3. Bottom-right: formulation F4.

6.2. Discontinuous solutions: 2d Burger's equation

We consider now the nonlinear 2d Burger's equation

$$\partial_t u + \partial_x\left(\frac{u^2}{2}\right) + \partial_y\left(\frac{u^2}{2}\right) = 0.$$

We solve the problem on the square $[-1,1]^2$ with the discontinuous initial solution

$$u_0 = \begin{cases} 1 & \text{if } x \in [-0.6,-0.1]\times[-0.35,0.15] \\ 0 & \text{otherwise} \end{cases}$$

The problem is solved up to the final time $t = 1$ on an unstructured triangulation with the topology shown on Fig. 3, and reference size $h \approx 1/80$. We compare the results of all the schemes considered. Only the simplest mass matrix form F1 (cf. Section 3) has been used.

We first consider the multidimensional upwind LDA and B schemes. The results for different RK schemes and lumping strategy are shown on Figs. 9–16. Concerning the LDA scheme, as one would expect, the solution exhibits oscillations near the discontinuities. These oscillations are much more pronounced when using selective lumping. More interesting are however the results of the B scheme, shown on Figs. 17–24. From all the contour plots we can see that the solution is smoother (the kinks close to the shock are less pronounced) when compared to the LDA scheme. When using selective lumping

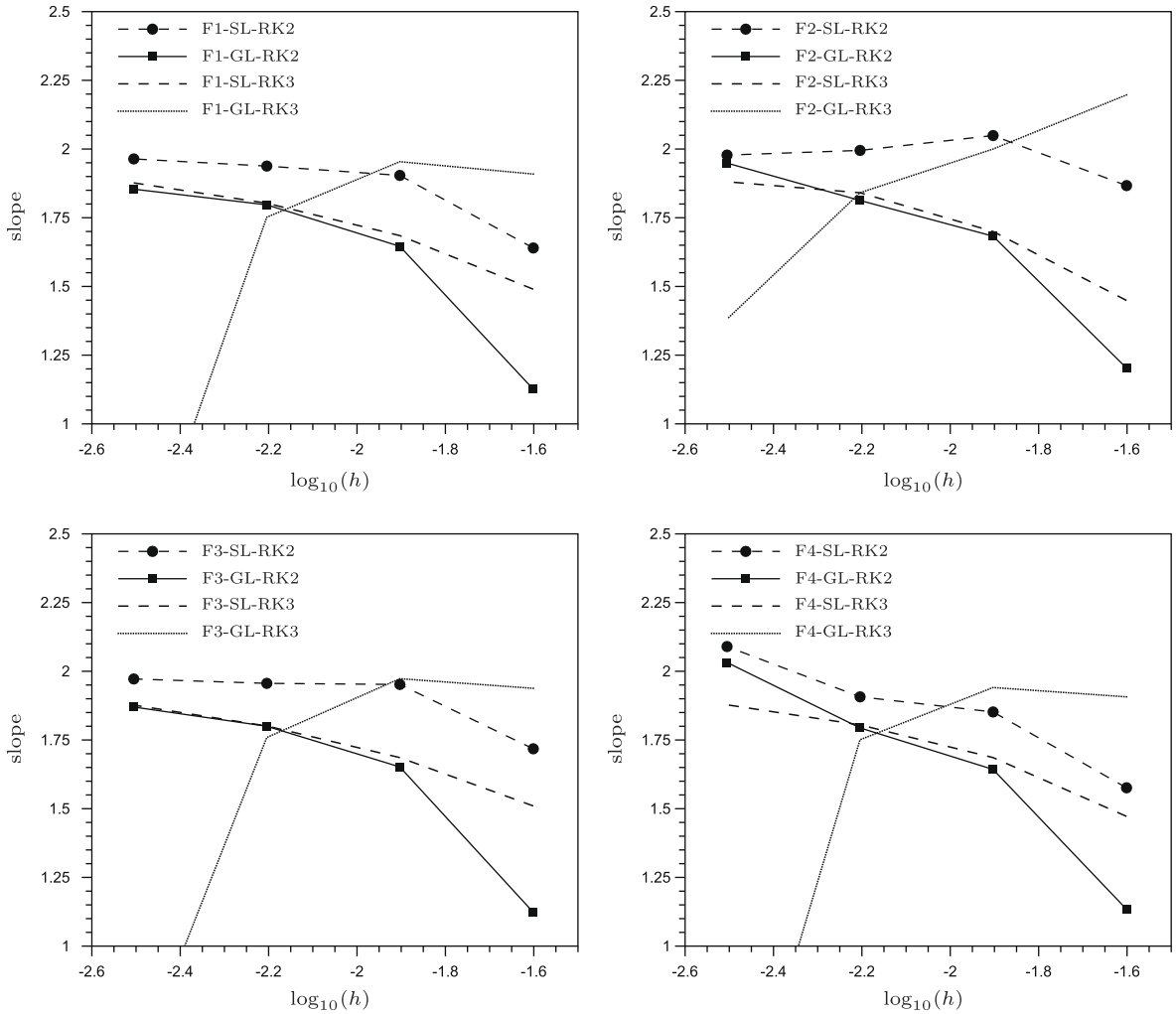

Fig. 5. Scalar advection: convergence rates for the LDA scheme. Top-left: formulation F1. Top-right: formulation F2. Bottom-left: formulation F3. Bottom-right: formulation F4.

oscillations still appear close to the discontinuity. This, as observed at the end of Section 5.2, is a consequence of the non-positive coefficients introduced by the Galerkin integral present when lumping selectively. A mixed formulation, in which these terms are also multiplied by the blending coefficient, might be used to cure the problem, but this is beyond the scopes of this paper and left for future work. The results obtained with global lumping show the expected monotone resolution of the discontinuities. Probably, the small negative undershoots can also be avoided by properly redefining the blending. Again, this is beyond the scopes of this paper and left for the future.

The results obtained with the centered distributions are displayed on Figs. 17–24. The qualitative behavior of these schemes is similar to the one of the multidimensional upwind discretizations. The linear SU scheme gives oscillations near the discontinuities. Milder oscillations are obtained when using global lumping. Concerning the Bc scheme, the results show smoother contours (the kinks close to the shock are less pronounced), and less oscillations. However, only the results obtained using global lumping show a monotone resolution of the moving shock.

We judge the results obtained on this nonlinear problem very encouraging : even without modifying the basic RD distribution, the nonlinear second order explicit RK–RD schemes can yield monotone solutions. This is further confirmed by the Euler results discussed hereafter.

7. Euler equations

As already said in Section 5, the extension of the schemes to the system of Euler equations is performed formally. As in the scalar case, the nonlinear schemes are not modified to take into account the additional terms coming from the explicit RK formulation and to improve their behavior close to discontinuities. For simplicity, only the schemes based on the simple

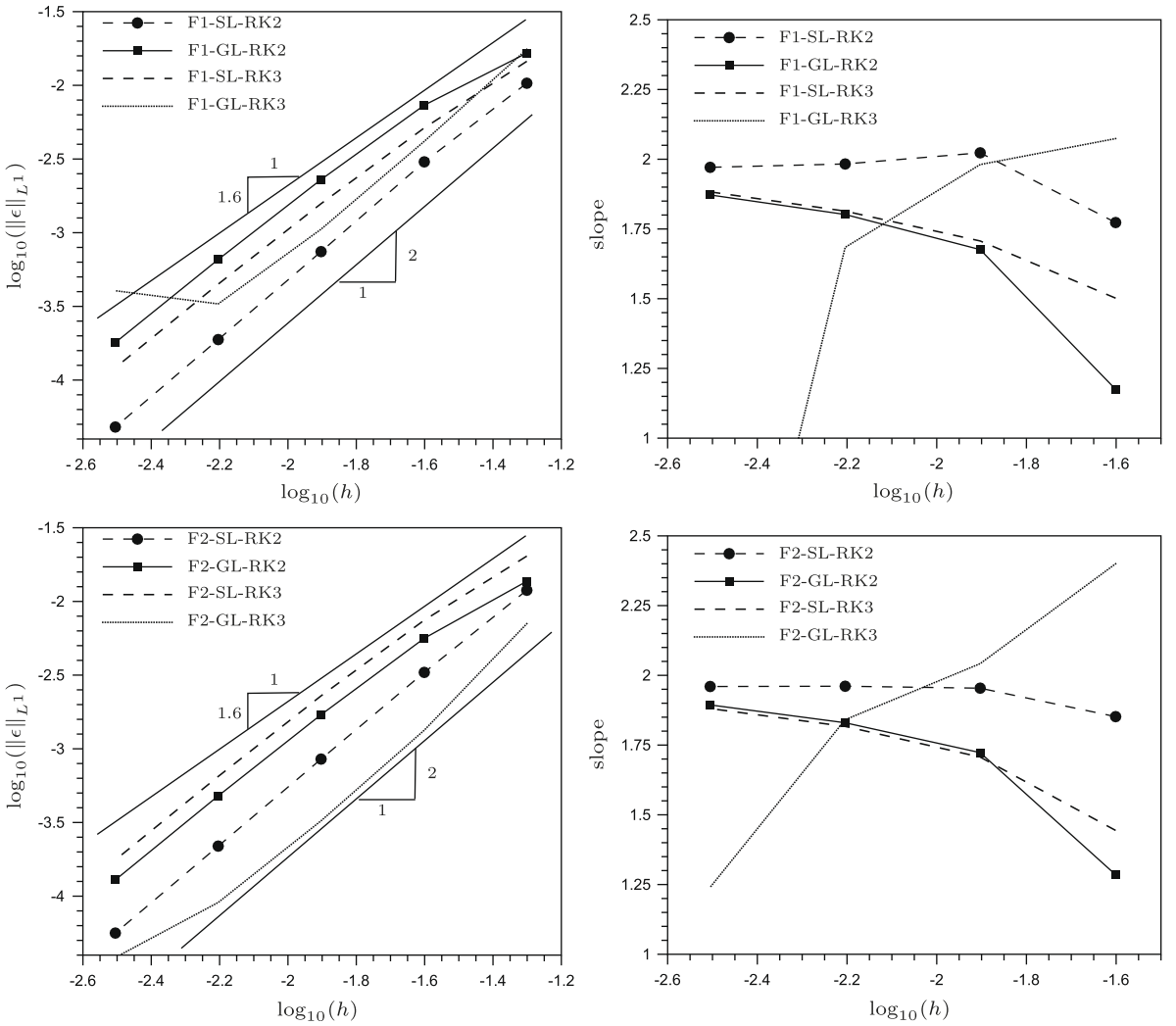

Fig. 6. Scalar advection: grid convergence for the SU scheme. Top row: formulation F1. Bottom row: formulation F2. Left column: convergence history. Right column: convergence rates.

mass matrix formulation F1 (cf. Section 3) are tested. The objective of the tests is to asses the accuracy of the discretizations, and the behavior of the nonlinear schemes in presence of a strong moving planar shock, and for more complex flow structures involving several contact lines and interactions between shocks and expansions.

7.1. Advection of a vortex: grid convergence

The accuracy of the schemes is measured on the advection of a constant density vortex. The test has been initially proposed in [21], to which we refer for all the details concerning its implementation. The solution involves the advection of a vortex with a constant density profile, and a smooth pressure variation of which the analytical form is known [21]. We solve the problem on a set of five unstructured grids with the topology shown on Fig. 3. The coarsest grid as a reference size of $h \approx 1/20$. The other meshes are obtained by means of four successive steps of conformal refinement. We measure the accuracy by means of the L^2 norm of the relative pressure error

$$\epsilon_p = \frac{p - p^{\text{exact}}}{p_\infty}$$

see [21] for the definition of p_∞ and of p^{exact}. The behavior of the L^∞ and L^1 norms is qualitatively and quantitatively very similar. The results are displayed on Figs. 25–28 in terms of error convergence history, and rate of convergence history. The results are qualitatively very similar to the ones discussed in Section 6.1. With the exception of the first refining step, we do obtain roughly second order of convergence with all the schemes except the RK3 ones when using global lumping.

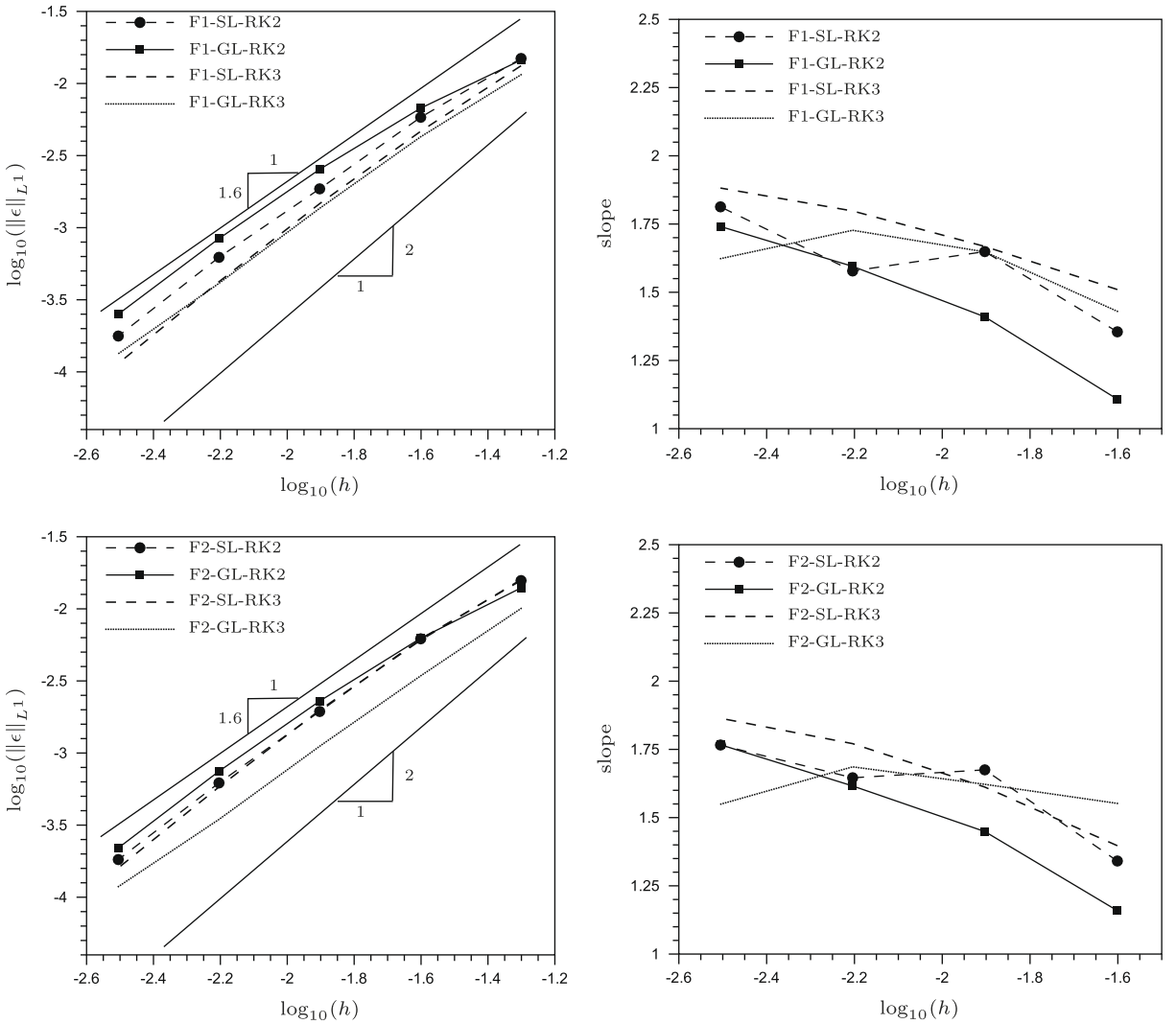

Fig. 7. Scalar advection: grid convergence for the B scheme. Top row: formulation F1. Bottom row: formulation F2. Left column: convergence history. Right column: convergence rates.

These schemes, exactly as in the scalar case, show a more or less evident decrease in accuracy, as the mesh is refined. The poor convergence rate at the first refinement step might be explained by the coarseness of the first meshes: the starting mesh only has 10 points through the vortex core, the second one 20 points. The drop in convergence rates of the RK3–GL schemes might be a consequence of a linear stability problem. This is under investigation.

The main difference between the distribution strategies is that the B scheme gives a slightly smaller asymptotic accuracy of about 1.7, while all the others attain convergence rates closer to 2. While this is expected for the linear schemes, we believe the face that the Bc scheme shows a better convergence is due to the definition of the entropy smoothness sensor $\delta(u_h)$ proposed in [2] and used for the blending, which really is turned on only very close to discontinuities. Once more, the improvement of the nonlinear schemes is a topic for future work. Nevertheless, the results obtained confirm once more our theoretical analysis.

7.2. Double Mach reflection

In this test we check the behavior of the nonlinear schemes in presence of a strong moving planar shock. The test case is that of a reflection of a Mach 10 oblique shock over a ramp proposed by Woodward and Colella in [42], to which we refer for details concerning the implementation. The computations have been run on an unstructured triangulation with the topology shown on Fig. 3 and reference mesh size $h \approx 1/100$.

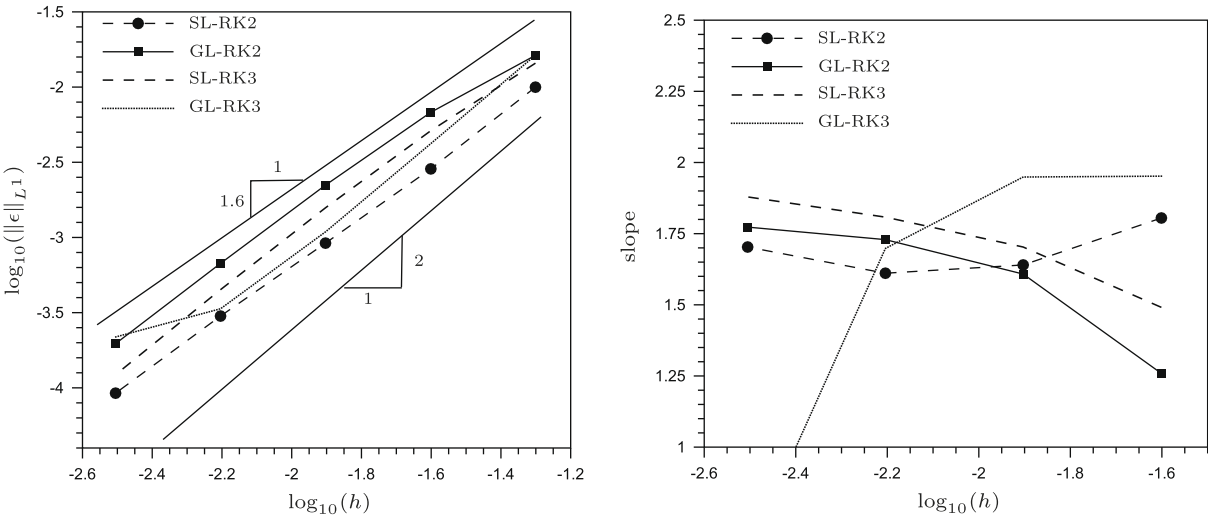

Fig. 8. Scalar advection: grid convergence for the Bc scheme. Left column: convergence history. Right column: convergence rates.

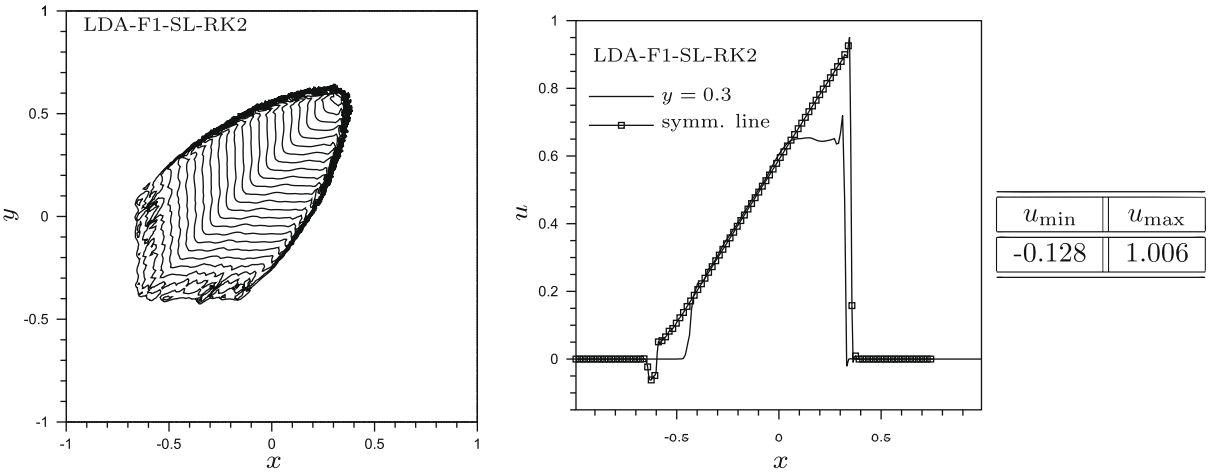

$u_{\min}$	$u_{\max}$
-0.128	1.006

Fig. 9. 2d Burger's equation: LDA–F1–SL–RK2 scheme. Left: contours at time $t = 1$. Middle: solution along the line $y = 0.3$ and along the symmetry line. Right: minimum and maximum values of the solution.

We display on Figs. 29 and 30 the density contours obtained with the B and Bc scheme, respectively. The first remark we can make is that even in presence of a strong moving shock both nonlinear discretizations yield quite smooth and non-oscillatory results. To confirm this we report on Figs. 31 and 32 the density and entropy distributions across the shock and on the wall, respectively. From Fig. 31 we see that the shock is resolved very sharply. Only a small overshoot in its vicinity is observed in almost all the solutions. An exception to this is the B scheme with RK3 time stepping and global lumping. In this case, as it can be also seen from the contour plot on Fig. 29 (bottom-right), we obtain some strange behavior in correspondence of the compression region where the bent incoming shock changes curvature. This seems to be a feature propagating from the upper boundary, where the exact shock movement is strongly imposed. This affects both the shock profile, as seen on Fig. 31, and the structures on the lower wall, as seen on Fig. 32. So far we have not been able to explain this behavior.

Apart from the above remarks, the solutions obtained are very satisfactory. The minimum and maximum values of the density, reported on Table 1 also show that the minimum of the density is always very close to 1.4 (its analytical value), again with the exception of the B-GL–RK3 scheme.

7.3. Mach 3 wind tunnel with a step

This final test is also taken from [42] and involves the formation and evolution of a moving shock in a Mach 3 wind tunnel with a step. We refer to [42] for details concerning the implementation of the test case. The mesh used for the computations

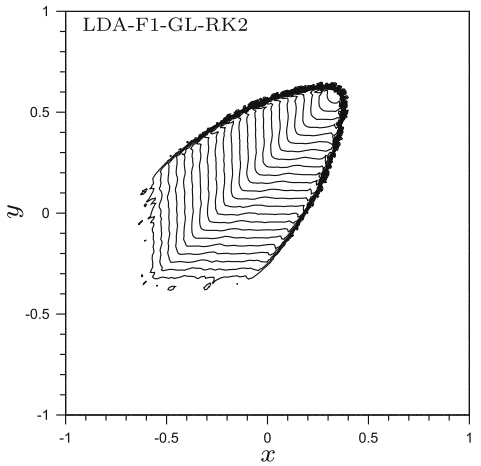

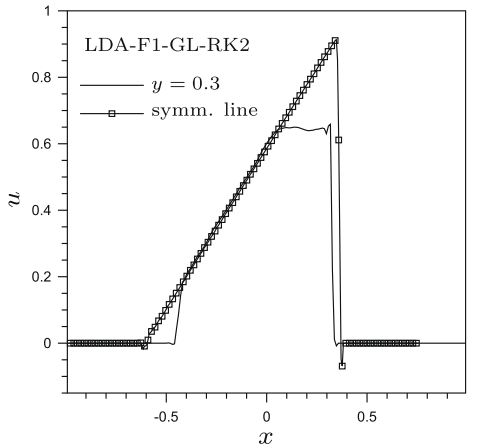

$u_{\min}$	$u_{\max}$
-0.144	0.951

Fig. 10. 2d Burger's equation: LDA–F1–GL–RK2 scheme. Left: contours at time $t = 1$. Middle: solution along the line $y = 0.3$ and along the symmetry line. Right: minimum and maximum values of the solution.

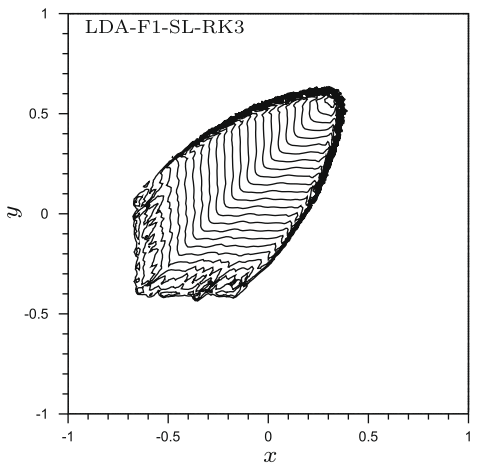

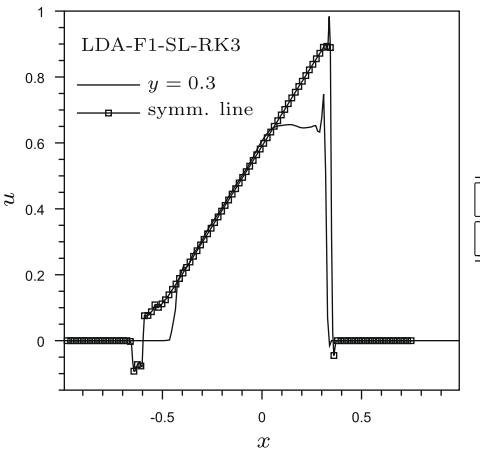

$u_{\min}$	$u_{\max}$
-0.144	1.081

Fig. 11. 2d Burger's equation: LDA–F1–SL–RK3 scheme. Left: contours at time $t = 1$. Middle: solution along the line $y = 0.3$ and along the symmetry line. Right: minimum and maximum values of the solution.

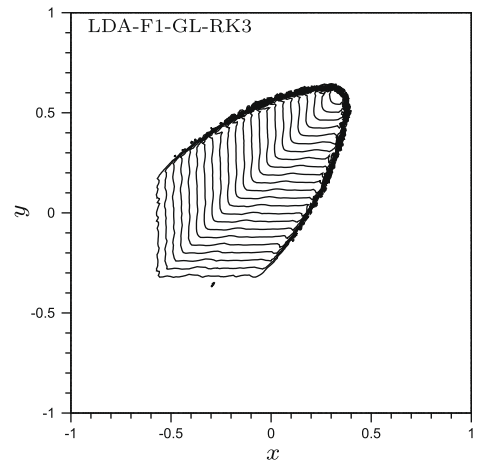

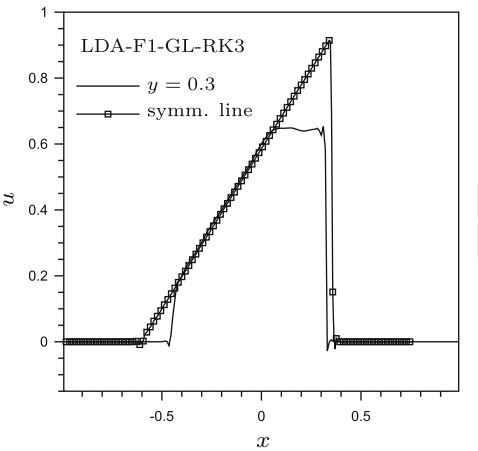

$u_{\min}$	$u_{\max}$
-0.243	0.952

Fig. 12. 2d Burger's equation: LDA–F1–GL–RK3 scheme. Left: contours at time $t = 1$. Middle: solution along the line $y = 0.3$ and along the symmetry line. Right: minimum and maximum values of the solution.

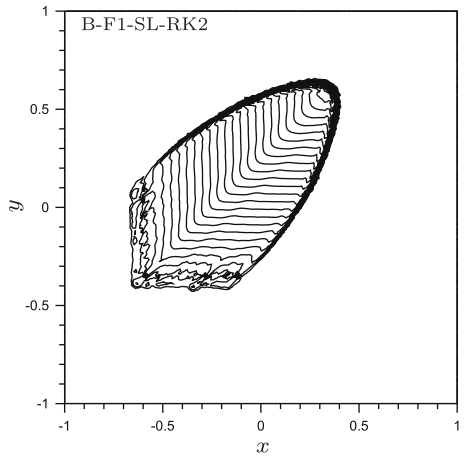

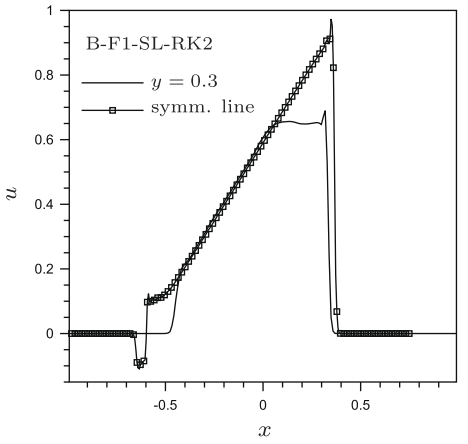

$u_{\min}$	$u_{\max}$
-0.134	1.018

Fig. 13. 2d Burger's equation: B–F1–SL–RK2 scheme. Left: contours at time $t = 1$. Middle: solution along the line $y = 0.3$ and along the symmetry line. Right: minimum and maximum values of the solution.

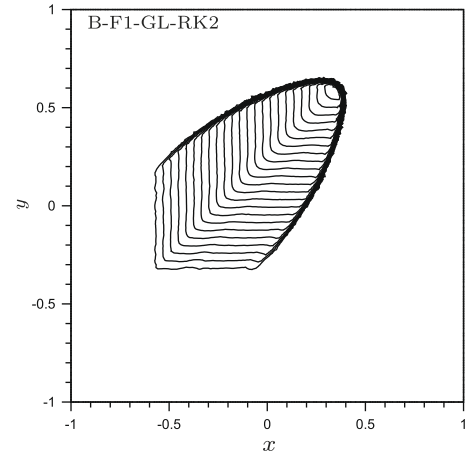

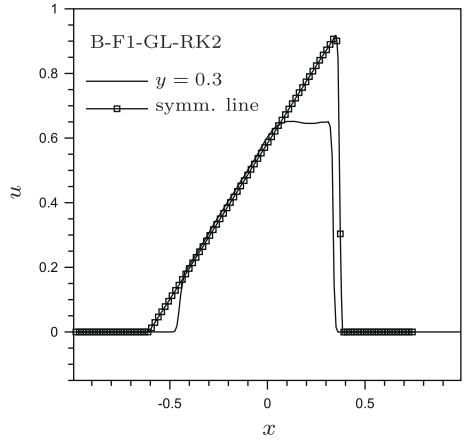

$u_{\min}$	$u_{\max}$
-0.004	0.920

Fig. 14. 2d Burger's equation: B–F1–GL–RK2 scheme. Left: contours at time $t = 1$. Middle: solution along the line $y = 0.3$ and along the symmetry line. Right: minimum and maximum values of the solution.

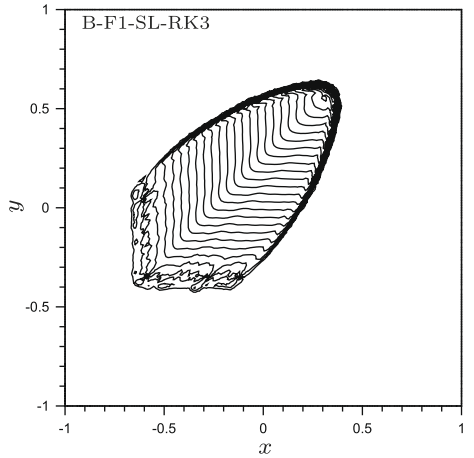

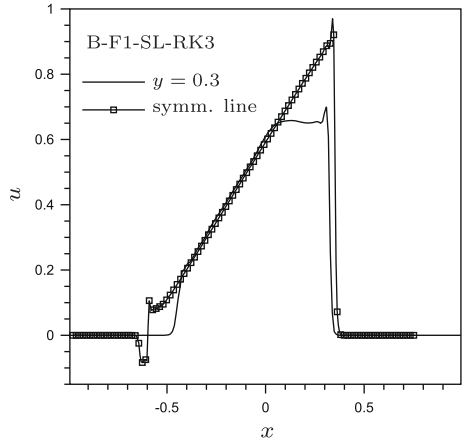

$u_{\min}$	$u_{\max}$
-0.121	1.002

Fig. 15. 2d Burger's equation: B–F1–SL–RK3 scheme. Left: contours at time $t = 1$. Middle: solution along the line $y = 0.3$ and along the symmetry line. Right: minimum and maximum values of the solution.

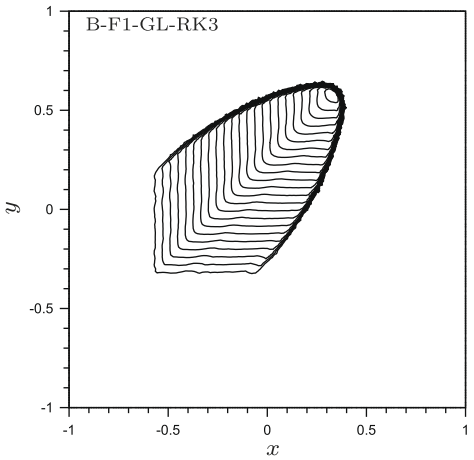

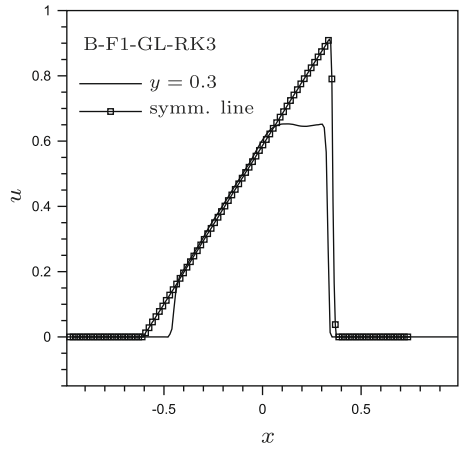

$u_{\min}$	$u_{\max}$
-0.027	0.913

Fig. 16. 2d Burger's equation: B–F1–GL–RK3 scheme. Left: contours at time $t = 1$. Middle: solution along the line $y = 0.3$ and along the symmetry line. Right: minimum and maximum values of the solution.

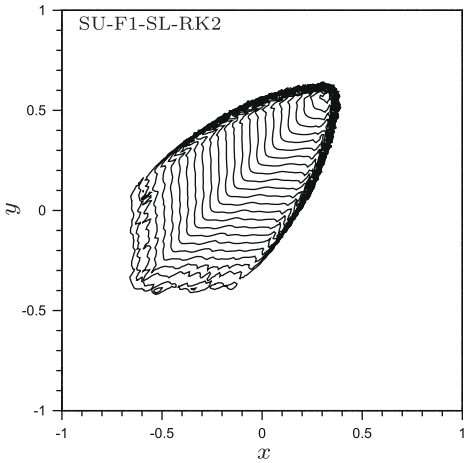

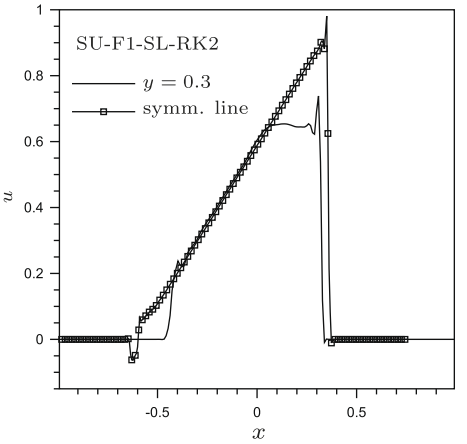

$u_{\min}$	$u_{\max}$
-0.103	1.064

Fig. 17. 2d Burger's equation: SU–F1–SL–RK2 scheme. Left: contours at time $t = 1$. Middle: solution along the line $y = 0.3$ and along the symmetry line. Right: minimum and maximum values of the solution.

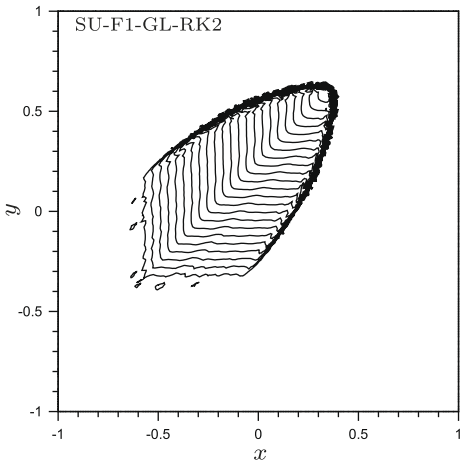

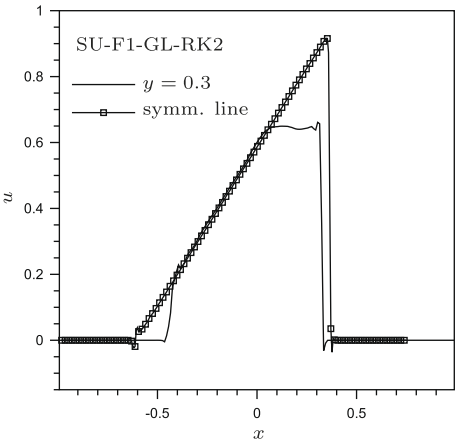

$u_{\min}$	$u_{\max}$
-0.146	0.969

Fig. 18. 2d Burger's equation: SU–F1–GL–RK2 scheme. Left: contours at time $t = 1$. Middle: solution along the line $y = 0.3$ and along the symmetry line. Right: minimum and maximum values of the solution.

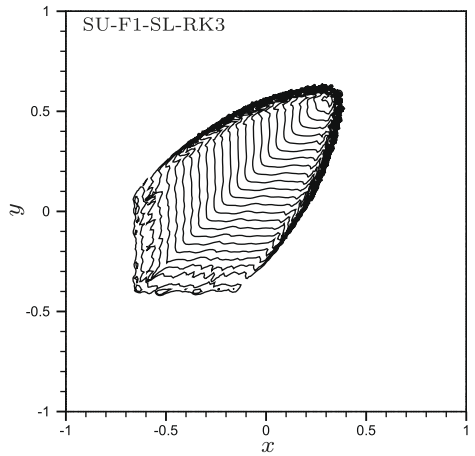

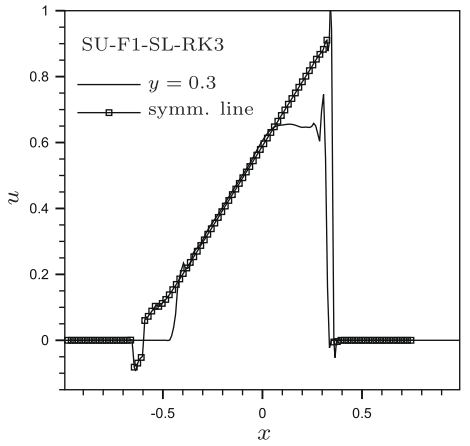

$u_{\min}$	$u_{\max}$
-0.110	1.113

Fig. 19. 2d Burger's equation: SU–F1–SL–RK3 scheme. Left: contours at time $t = 1$. Middle: solution along the line $y = 0.3$ and along the symmetry line. Right: minimum and maximum values of the solution.

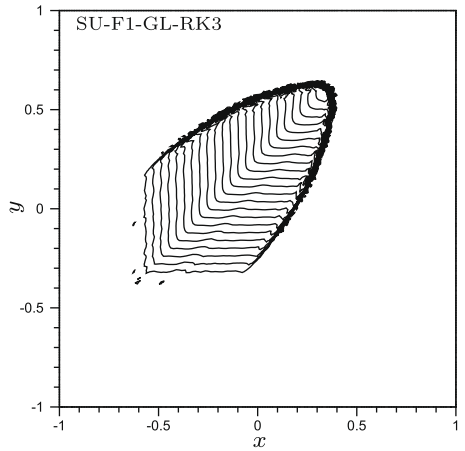

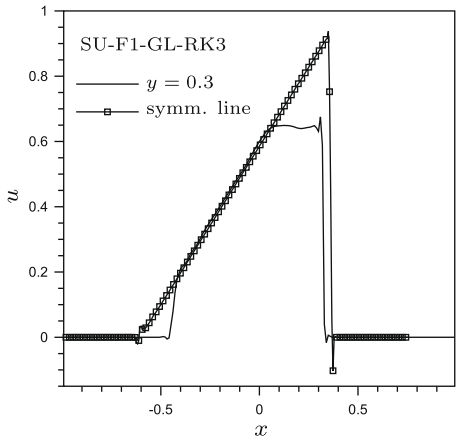

$u_{\min}$	$u_{\max}$
-0.211	0.985

Fig. 20. 2d Burger's equation: SU–F1–GL–RK3 scheme. Left: contours at time $t = 1$. Middle: solution along the line $y = 0.3$ and along the symmetry line. Right: minimum and maximum values of the solution.

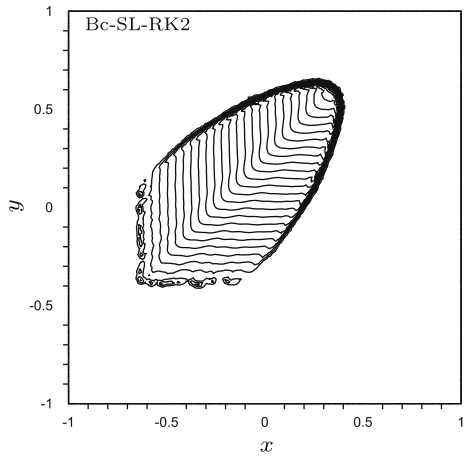

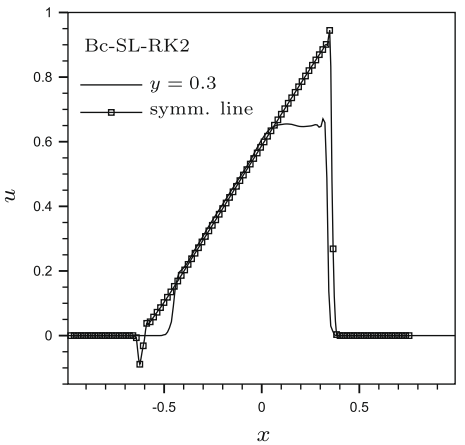

$u_{\min}$	$u_{\max}$
-0.131	0.973

Fig. 21. 2d Burger's equation: Bc–SL–RK2 scheme. Left: contours at time $t = 1$. Middle: solution along the line $y = 0.3$ and along the symmetry line. Right: minimum and maximum values of the solution.

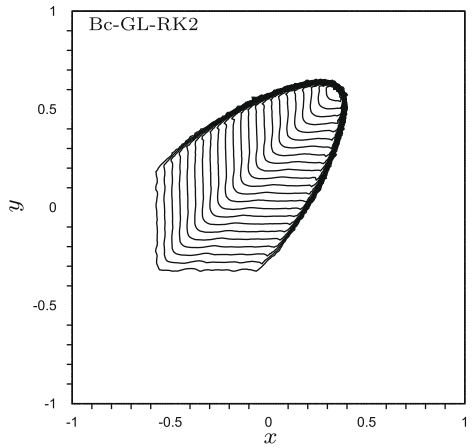

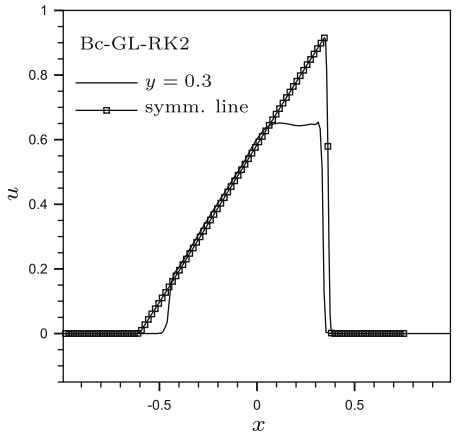

$u_{\min}$	$u_{\max}$
-0.014	0.919

Fig. 22. 2d Burger's equation: Bc–GL–RK2 scheme. Left: contours at time $t = 1$. Middle: solution along the line $y = 0.3$ and along the symmetry line. Right: minimum and maximum values of the solution.

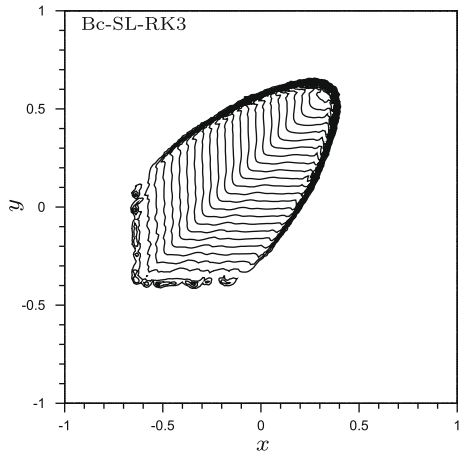

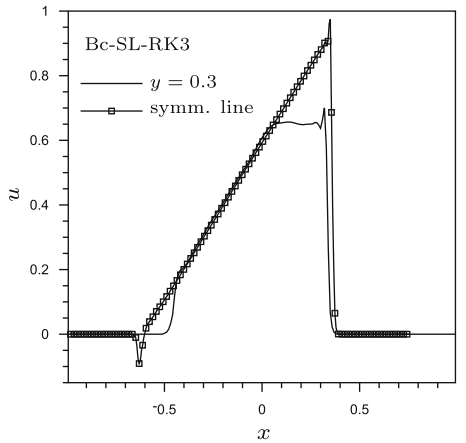

$u_{\min}$	$u_{\max}$
-0.135	1.017

Fig. 23. 2d Burger's equation: Bc–SL–RK3 scheme. Left: contours at time $t = 1$. Middle: solution along the line $y = 0.3$ and along the symmetry line. Right: minimum and maximum values of the solution.

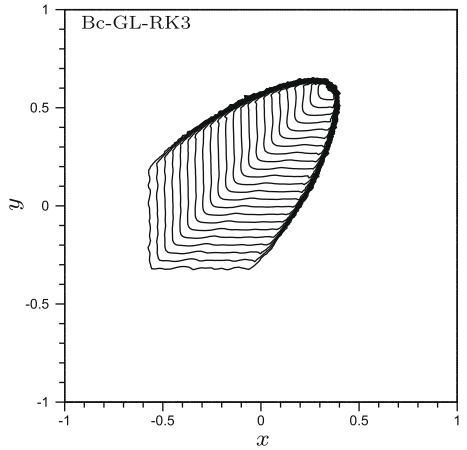

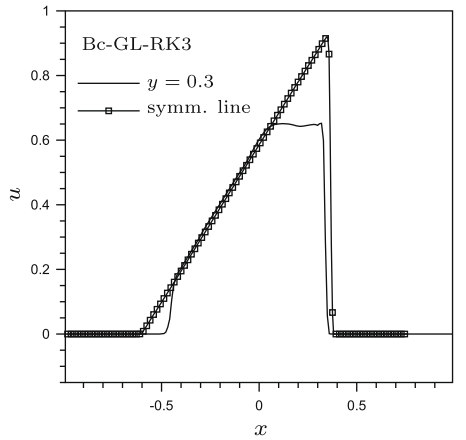

$u_{\min}$	$u_{\max}$
-0.013	0.929

Fig. 24. 2d Burger's equation: Bc–GL–RK3 scheme. Left: contours at time $t = 1$. Middle: solution along the line $y = 0.3$ and along the symmetry line. Right: minimum and maximum values of the solution.

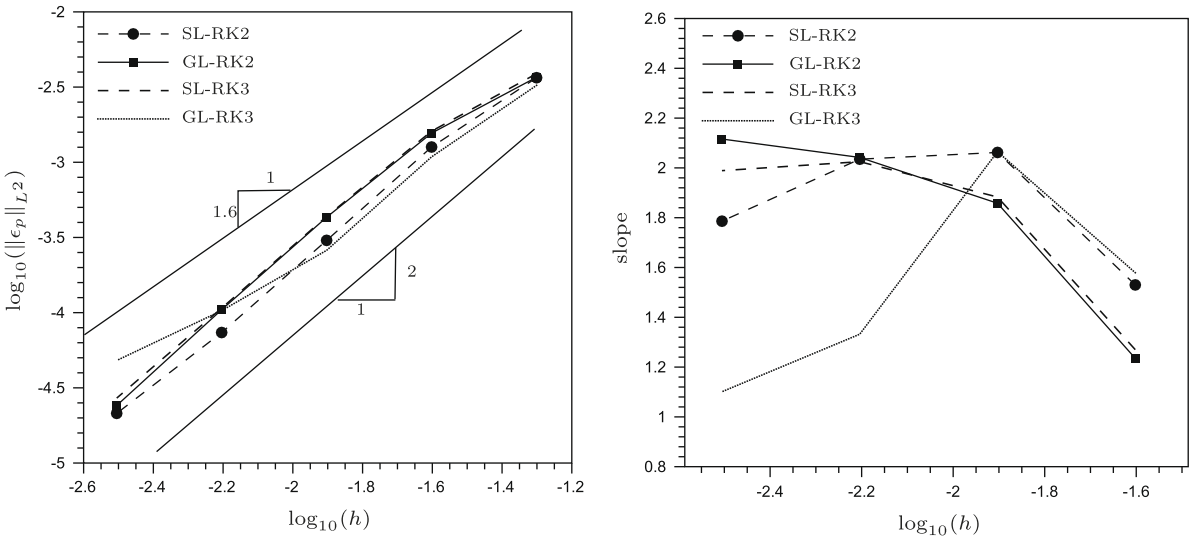

Fig. 25. Vortex advection: grid convergence for the LDA scheme with F1. Left column: convergence history. Right column: convergence rates.

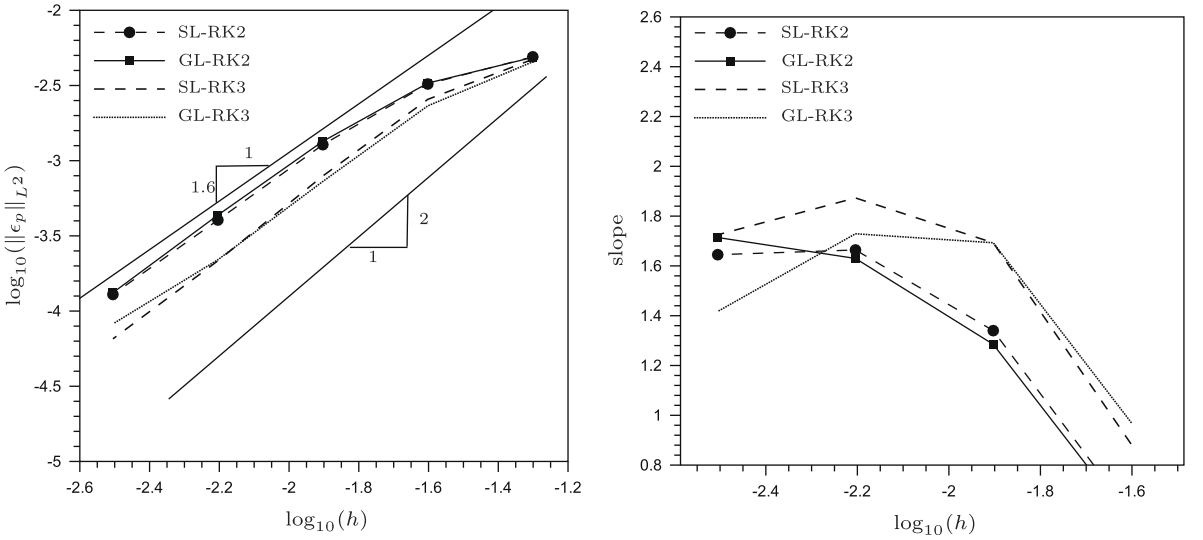

Fig. 26. Vortex advection: grid convergence for the B scheme with F1. Left column: convergence history. Right column: convergence rates.

is the same used in [15,17]. A close up view in vicinity of the corner of the step is displayed on Fig. 33. The reference mesh size far from the corner is $h \approx 1/80$. The mesh is refined at the corner to attain a minimum size of $h \approx 1/1000$. No particular numerical treatment has been used near the corner to handle the supersonic expansion taking place during the transient.

The solutions obtained at times $t = 0.5$, $t = 1.5$, and $t = 4.0$ with the B and Bc schemes are shown on Figs. 34–41. All the figures show a monotone and sharp resolution of the shocks, and of the contact lines. The non-oscillatory character of the results is confirmed by the line plots of the solution along the upper wall of the step (line $y = 0.2$ containing the corner singularity). We never obtained negative densities. Note that this is a test case where the explicit formulation does give an advantage with respect to the implicit schemes based on Crank–Nicholson time integration [4,33]. Even if implicit in time, the positivity of the schemes proposed in the last references is still guaranteed by an explicit type time step restriction which, in presence of mesh refinement, renders the implicit formulation extremely time consuming.

As a last remark, we note that the Bc scheme with selective lumping yields a much better resolution of the flow, as seen for example from the kinks of the initial shock (top-left on Figs. 38 and 39), and from the resolution of the contact emanating from the interaction of the corner expansion with the reflected shock (middle-left on Figs. 38 and 39).

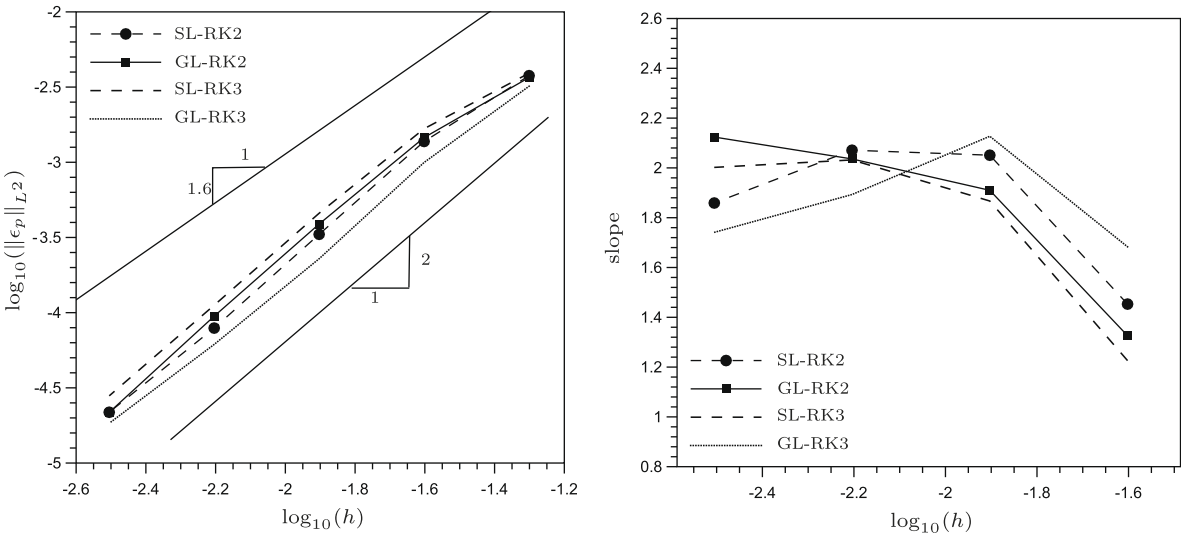

Fig. 27. Vortex advection: grid convergence for the SU scheme with F1. Left column: convergence history. Right column: convergence rates.

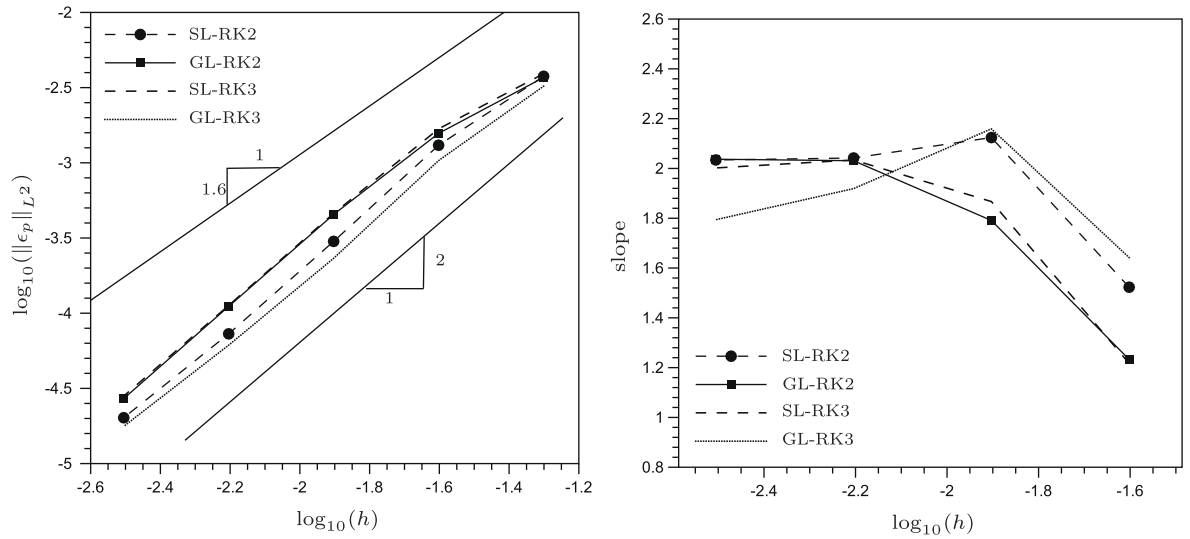

Fig. 28. Vortex advection: grid convergence for the Bc scheme. Left column: convergence history. Right column: convergence rates.

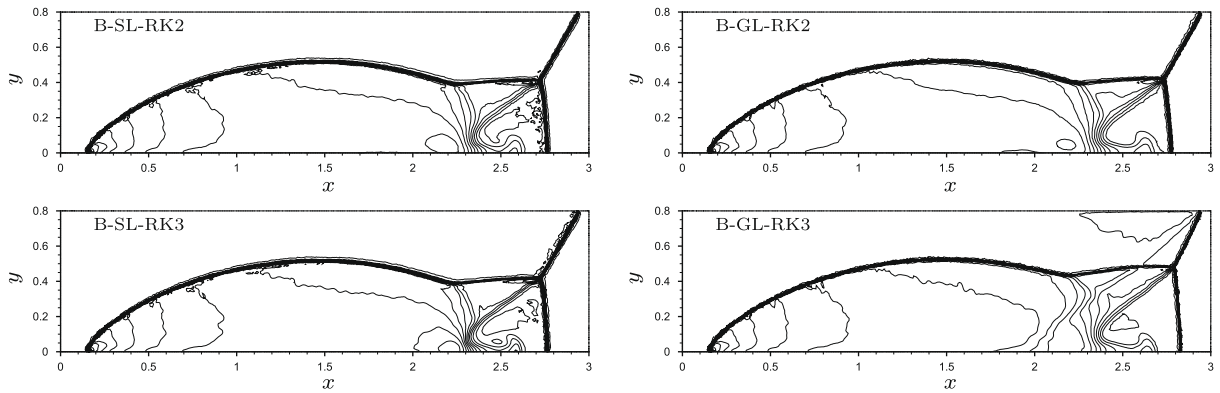

Fig. 29. Double Mach reflection. Density contours for the B scheme. 30 equally spaced contours from 1 to 24. Top row: RK2. Bottom row: RK3. Left column: selective lumping. Right column: global lumping.

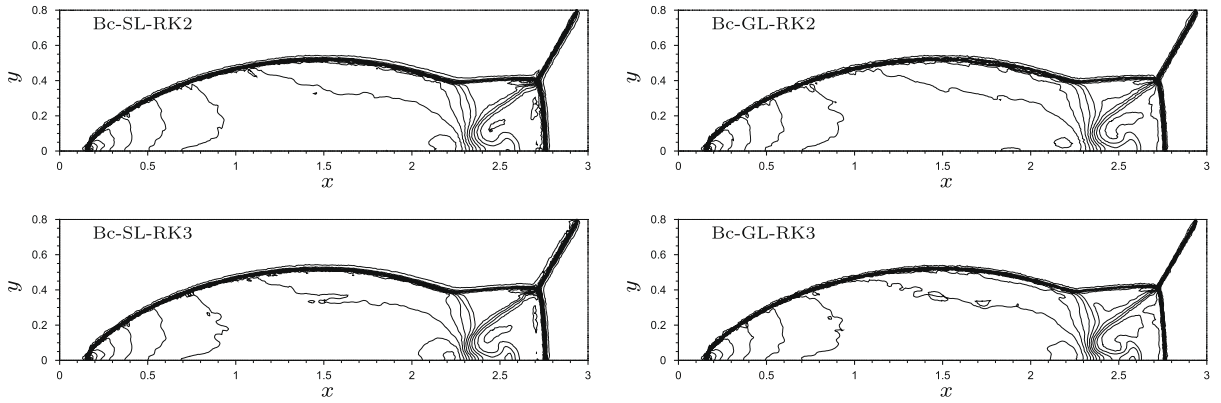

Fig. 30. Double Mach reflection. Density contours for the Bc scheme. 30 equally spaced contours from 1 to 24. Top row: RK2. Bottom row: RK3. Left column: selective lumping. Right column: global lumping.

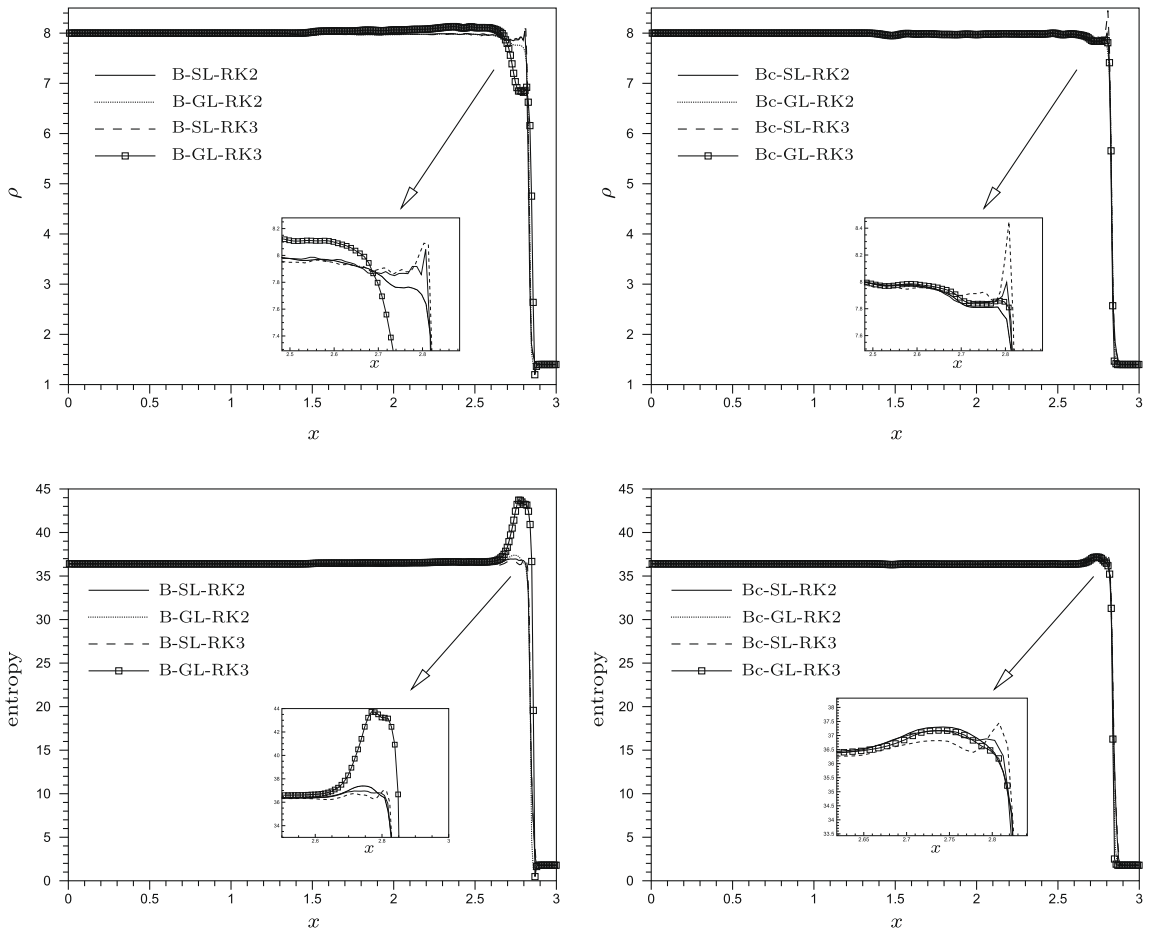

Fig. 31. Double Mach reflection. Solution across the oblique shock ($y = 0.6$). Top row: density. Bottom row: entropy. Left column: B scheme. Right column: Bc scheme.

8. Conclusions

In this paper, we have described a strategy to construct explicit second order Residual Distribution schemes based on Runge–Kutta time integration. The final discrete equations are obtained through three steps: recasting RD as stabilized

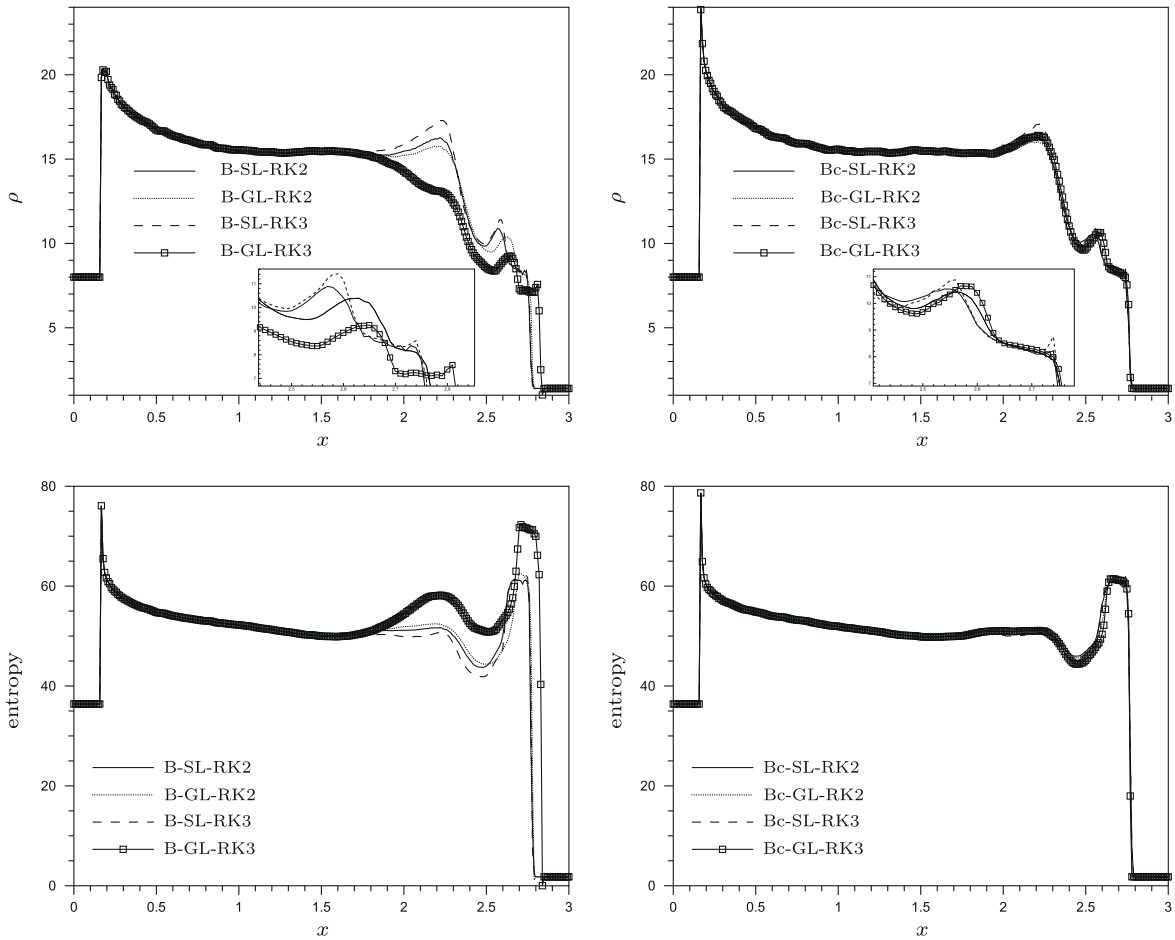

Fig. 32. Double Mach reflection. Solution along the wall ($y = 0$). Top row: density. Bottom row: entropy. Left column: B scheme. Right column: Bc scheme.

Table 1
Double Mach reflection: minimum and maximum values of the density. Left: B scheme. Right: Bc scheme.

	ρ_{min}	$\rho_{\max}$
B–SL–RK2	1.40	22.30
B–SL–RK3	1.29	22.30
B–GL–RK2	1.37	22.30
B–GL–RK3	0.77	22.20
Bc–SL–RK2	1.398	24.12
Bc–SL–RK3	1.4	24.07
Bc–GL–RK2	1.397	24.00
Bc–GL–RK3	1.396	23.98

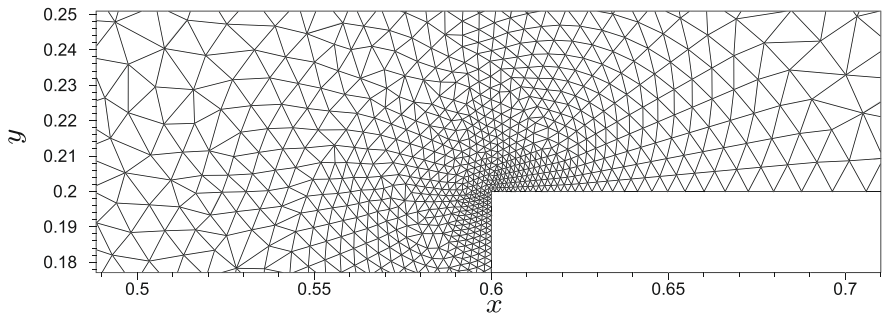

Fig. 33. Mach 3 wind tunnel: close-up view of the mesh around the corner ($h = 1/80$ far from the corner, $h = 10^{-3}$ at the corner).

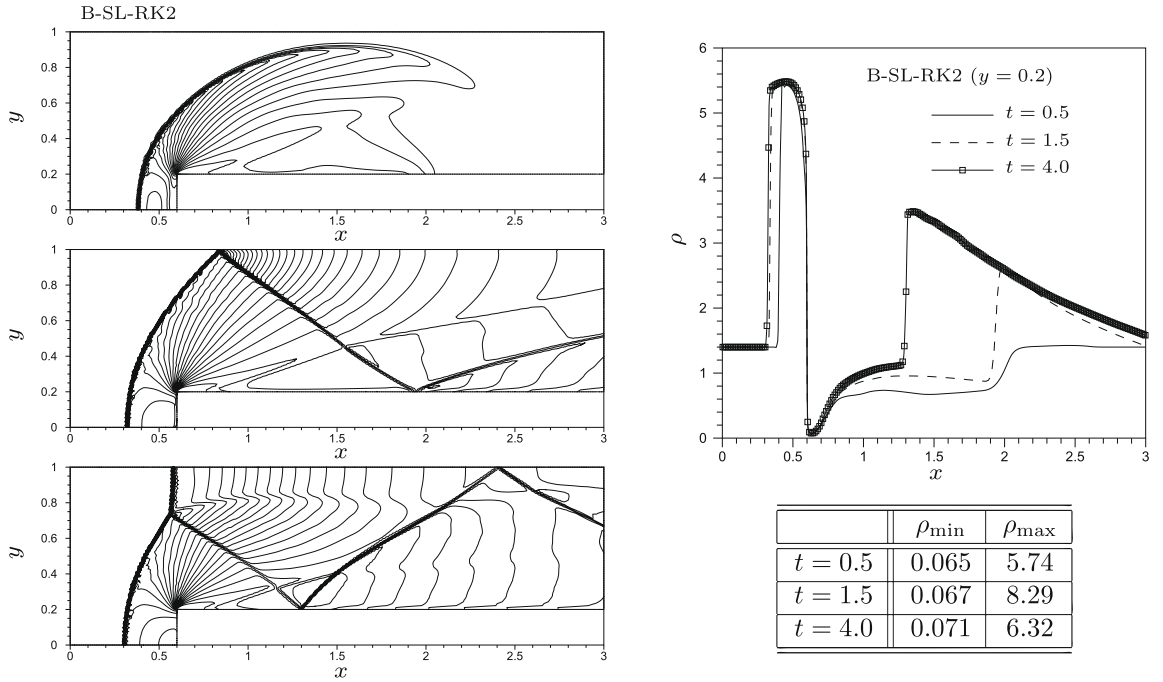

	$\rho_{\min}$	$\rho_{\max}$
$t = 0.5$	0.065	5.74
$t = 1.5$	0.067	8.29
$t = 4.0$	0.071	6.32

Fig. 34. Mach 3 wind tunnel: B–SL–RK2 scheme. Left: density contours at time $t = 0.5$ (top), $t = 1.5$ (middle), and $t = 4.0$ (bottom); 30 equally spaced contours between 0.5 and 8. Right: density distribution along the line $y = 0.2$, and minimum and maximum values of the density.

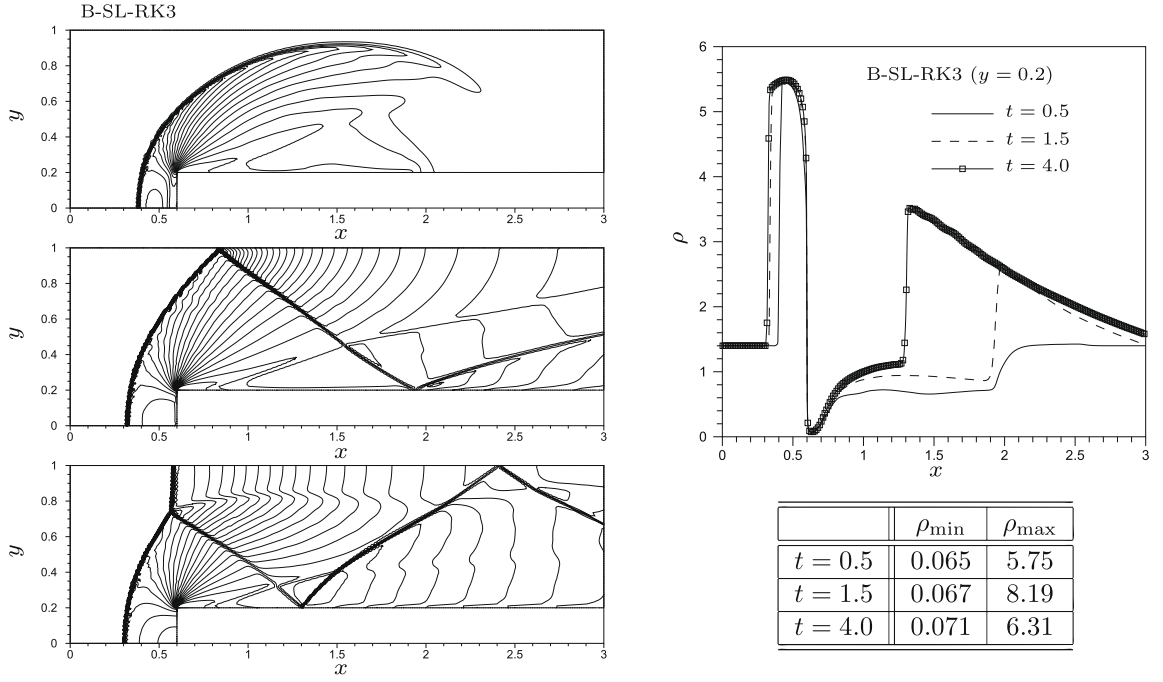

	$\rho_{\min}$	$\rho_{\max}$
$t = 0.5$	0.065	5.75
$t = 1.5$	0.067	8.19
$t = 4.0$	0.071	6.31

Fig. 35. Mach 3 wind tunnel: B–SL–RK3 scheme. Left: density contours at time ($t = 0.5$ (top), $t = 1.5$ (middle), and $t = 4.0$ (bottom); 30 equally spaced contours between 0.5 and 8. Right: density distribution along the line $y = 0.2$, and minimum and maximum values of the density.

Galerkin schemes, introducing a time-shifted residual in the RD stabilization, using high order mass lumping to obtain a fully explicit update. All the theoretical arguments justifying our construction have been thoroughly discussed, and strong numerical evidence has been given to confirm them.

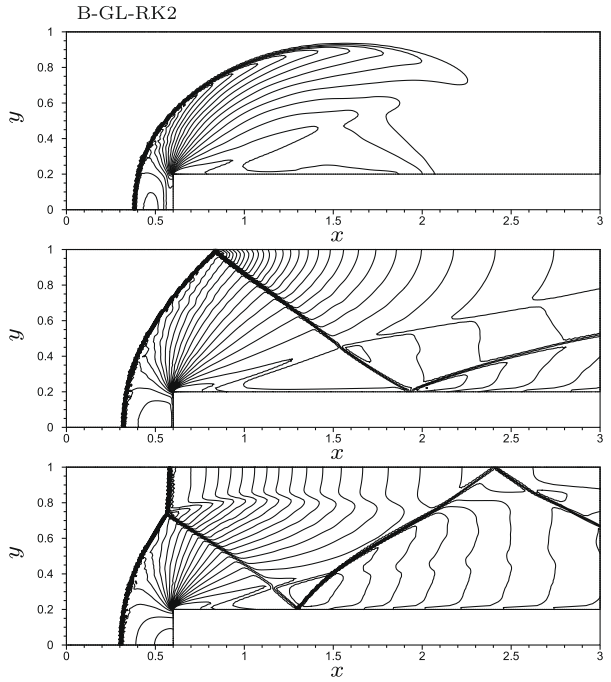

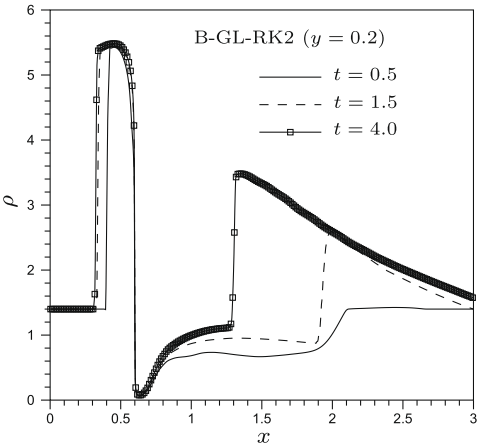

	$\rho_{\min}$	$\rho_{\max}$
$t = 0.5$	0.062	5.73
$t = 1.5$	0.067	7.89
$t = 4.0$	0.072	6.29

Fig. 36. Mach 3 wind tunnel: B–GL–RK2 scheme. Left: density contours at time ($t = 0.5$ (top), $t = 1.5$ (middle), and $t = 4.0$ (bottom); 30 equally spaced contours between 0.5 and 8. Right: density distribution along the line $y = 0.2$, and minimum and maximum values of the density.

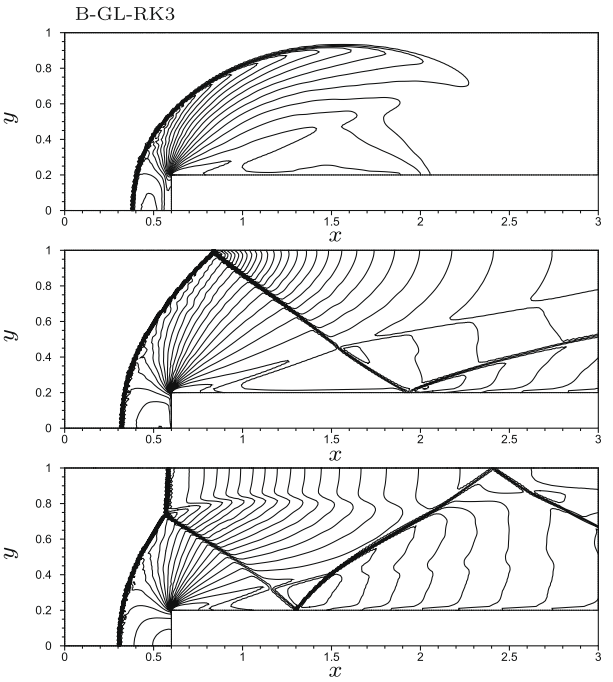

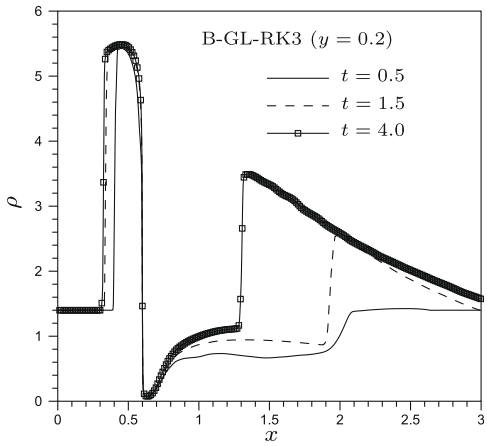

	$\rho_{\min}$	$\rho_{\max}$
$t = 0.5$	0.062	5.73
$t = 1.5$	0.067	7.86
$t = 4.0$	0.072	6.30

Fig. 37. Mach 3 wind tunnel: B–GL–RK3 scheme. Left: density contours at time ($t = 0.5$ (top), $t = 1.5$ (middle), and $t = 4.0$ (bottom); 30 equally spaced contours between 0.5 and 8. Right: density distribution along the line $y = 0.2$, and minimum and maximum values of the density.

The numerical results are extremely encouraging both concerning accuracy, and monotonicity. We think this work paves the way for a different class of RD schemes based on explicit, or mixed, time integration where the RD mass matrix does not necessarily need to be inverted.

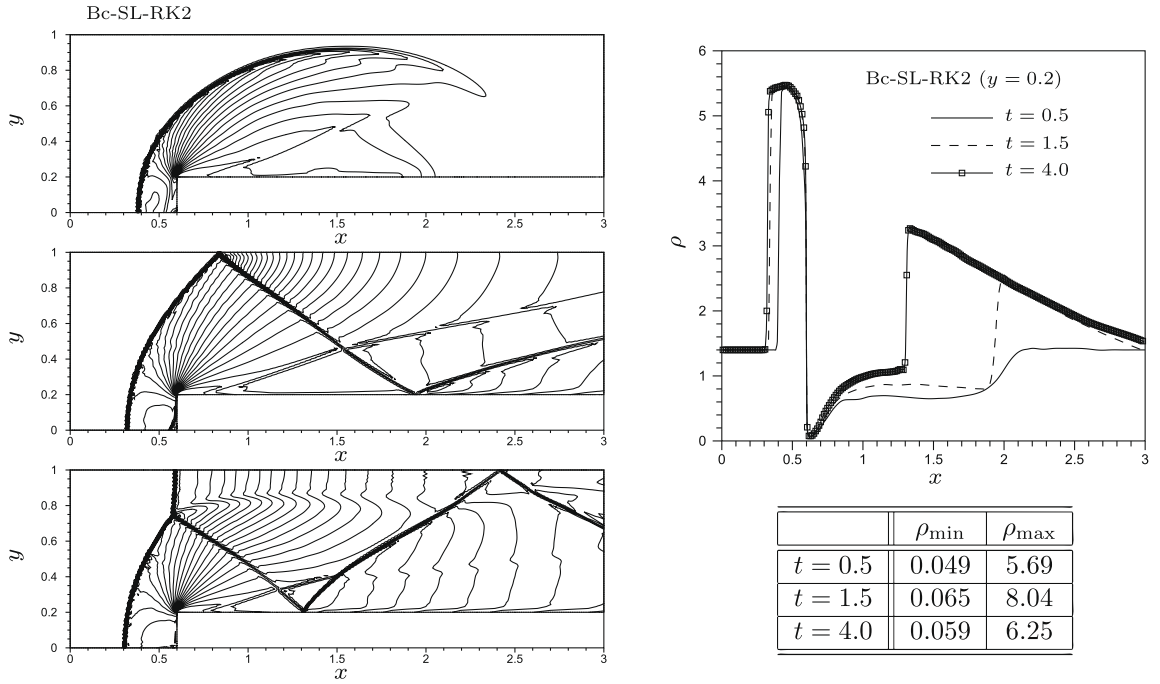

	$\rho_{\min}$	$\rho_{\max}$
$t = 0.5$	0.049	5.69
$t = 1.5$	0.065	8.04
$t = 4.0$	0.059	6.25

Fig. 38. Mach 3 wind tunnel: Bc-SL-RK2 scheme. Left: density contours at time ($t = 0.5$ (top), $t = 1.5$ (middle), and $t = 4.0$ (bottom); 30 equally spaced contours between 0.5 and 8. Right: density distribution along the line $y = 0.2$, and minimum and maximum values of the density.

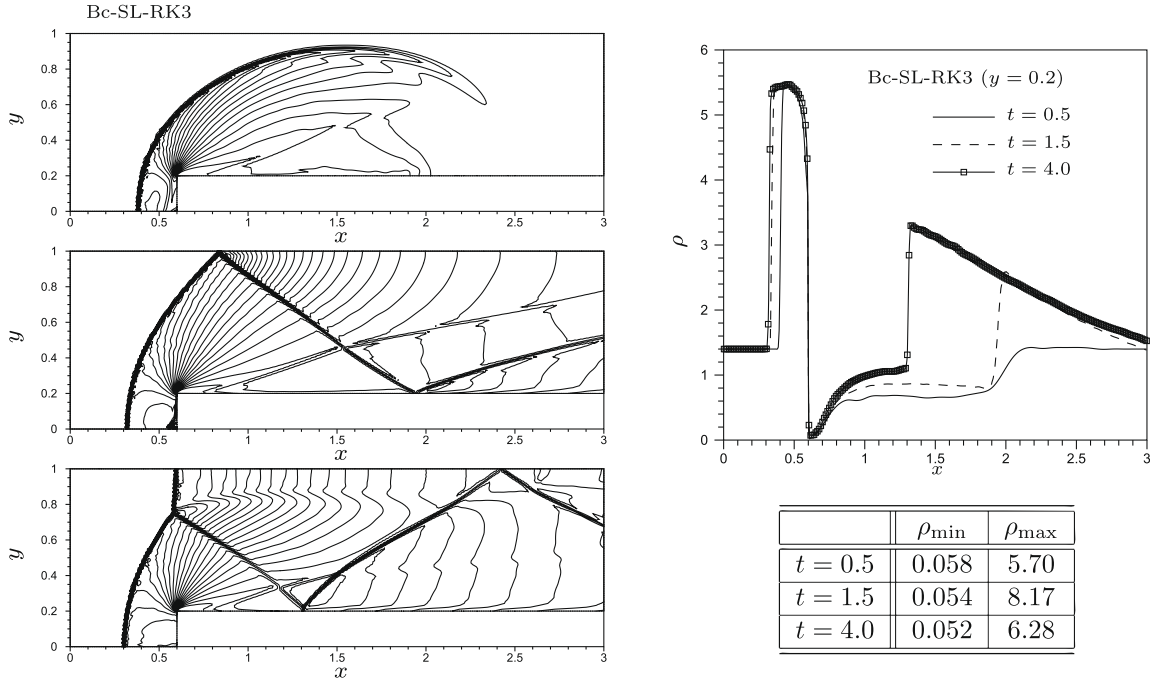

	$\rho_{\min}$	$\rho_{\max}$
$t = 0.5$	0.058	5.70
$t = 1.5$	0.054	8.17
$t = 4.0$	0.052	6.28

Fig. 39. Mach 3 wind tunnel: Bc–SL–RK3 scheme. Left: density contours at time ($t = 0.5$ (top), $t = 1.5$ (middle), and $t = 4.0$ (bottom); 30 equally spaced contours between 0.5 and 8. Right: density distribution along the line $y = 0.2$, and minimum and maximum values of the density.

Concerning the developments of the work reported in this paper, we mention the following points:

- We are currently performing a Fourier analysis on structured triangulations to better understand the linear stability properties of the linear schemes, when using different forms of the mass matrix, and also to understand the influence of the type of lumping on the stability of the resulting scheme.

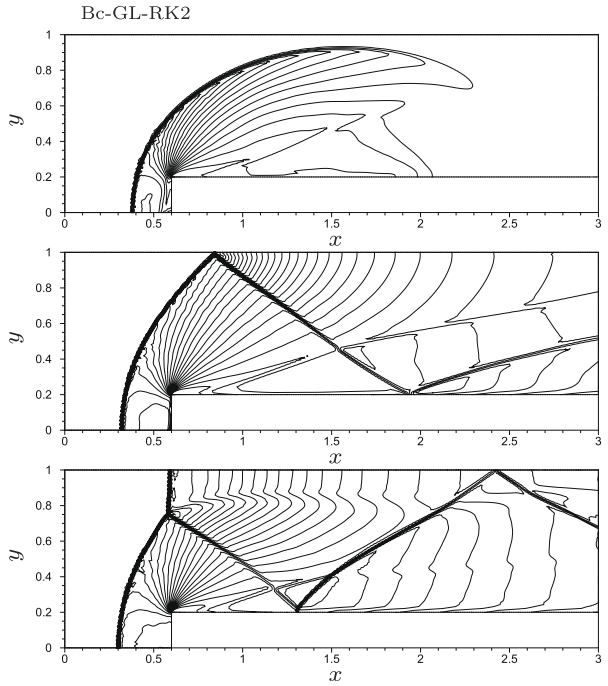

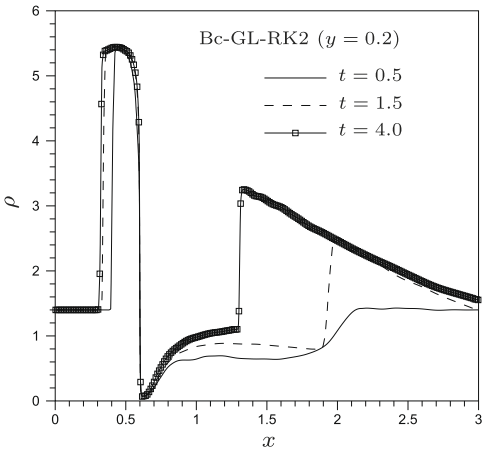

	$\rho_{\min}$	$\rho_{\max}$
$t = 0.5$	0.062	5.68
$t = 1.5$	0.059	7.88
$t = 4.0$	0.058	6.31

Fig. 40. Mach 3 wind tunnel: Bc–GL–RK2 scheme. Left: density contours at time ($t = 0.5$ (top), $t = 1.5$ (middle), and $t = 4.0$ (bottom); 30 equally spaced contours between 0.5 and 8. Right: density distribution along the line $y = 0.2$, and minimum and maximum values of the density.

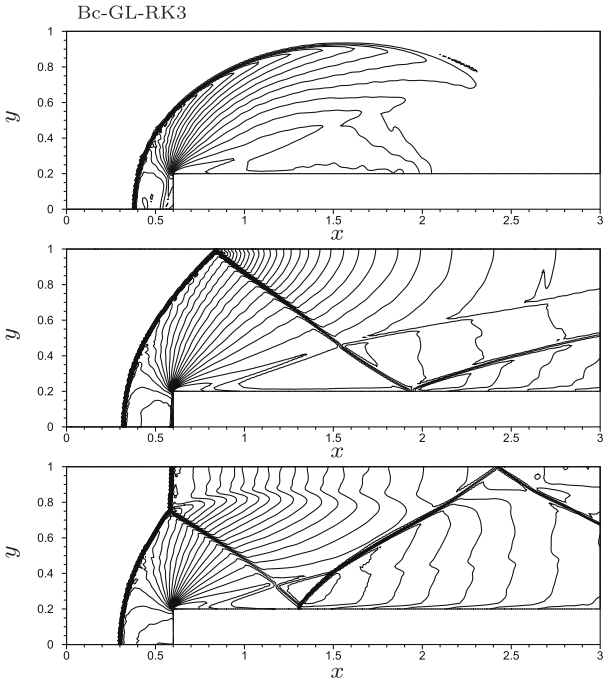

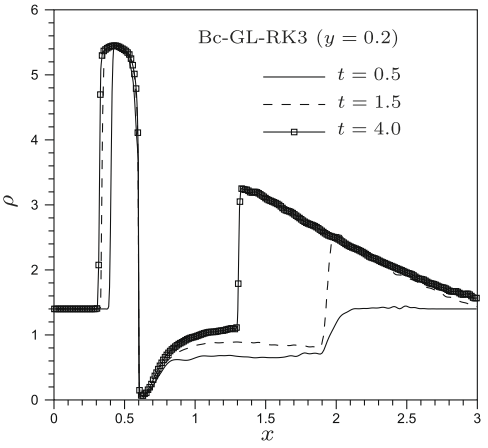

	$\rho_{\min}$	$\rho_{\max}$
$t = 0.5$	0.055	5.70
$t = 1.5$	0.063	7.87
$t = 4.0$	0.045	6.33

Fig. 41. Mach 3 wind tunnel: Bc–GL–RK3 scheme. Left: density contours at time ($t = 0.5$ (top), $t = 1.5$ (middle), and $t = 4.0$ (bottom); 30 equally spaced contours between 0.5 and 8. Right: density distribution along the line $y = 0.2$, and minimum and maximum values of the density.

- Even though we judge the results presented here quite satisfactory (especially for the Euler equations) there is definitely space to improve the nonlinear schemes, taking into account the fully discrete RK time-stepping and the terms arising from mass lumping in the positivity analysis.

- An immediate application of the explicit RK–RD schemes is given by the Shallow Water equations where the preservation of the positivity of the depth leads, for the standard implicit RD, to a strict constraint on the time step [32]. We think the RK–RD approach proposed would represent an improvement, still preserving most of the nice properties of the RD discretization.
- The extension to more than second order should be relatively straight forward when making use of higher order elements allowing higher order mass lumping. From this point of view we will profit of the work that has been done on the wave equation (see *e.g.* [23,39] and references therein).
- The technique described here can also be used in conjunction with discontinuous data representation. In particular, our approach gives a means of extending the discontinuous RD schemes proposed in [7,27] without the need of inverting the local RD mass matrix. Higher order variants of these explicit discontinuous RD schemes can be obtained using local finite element spaces borrowed from [23,39].
- It will definitely very interesting to see how the high order version of these RK–RD schemes (with continuous or discontinuous space approximations) perform in terms of accuracy and shock capturing when compared to other higher order discretization approaches such as *e.g.* the Runge–Kutta Discontinuous Galerkin schemes [13], or the spectral finite volume method of [41].

Acknowledgments

We are grateful to G. Scovazzi (SANDIA NL, Albuquerque) for his numerous remarks on the solution of the nonlinear Newton loop in RD discretizations, and for pointing out the relations with predictor–multi-corrector schemes used in SUPG discretizations. The authors have been partly funded by the EU Strep ADIGMA (Contract AST5-CT-2006-030719). RA has been funded by the ERC Grant ADECCO (Grant Agreement No. 226316).

Appendix A. Proof of Proposition 4.3

We derive a sufficient condition on the $\bar{r}^k$ guaranteeing that the accuracy of the Runge–Kutta Galerkin approximation is not lost when adding the bubble contribution. To do this we use a truncation error analysis, following the approach of [31]. What we want to do is to show that for a pth order spatial approximation, and when employing a pth order RK scheme, the solution at time t^n verifies a truncation error equation of the type $\mathcal{E}_n \leqslant C_n h^p$. A global space–time truncation error estimate can then be obtained by integrating over each time interval and adding up over all the time slabs.

To do this we consider a more general polynomial approximation in space. The degrees of freedom are still approximations of the values of the unknown in some nodal locations of the mesh, except that, differently from the P^1 case, these are the element vertices plus other locations, as for example in standard P^k elements, or in more "exotic" polynomial spaces, such as the ones proposed in [23,39,38]. As before, we denote by φ_i the basis functions spanning the polynomial space, by u_h the spatial approximation of a function u, and with K we denote the total number of degrees of freedom (DoF) contained in an element of the mesh.

We start by recalling that, given a smooth classical solution of the problem w, Hypothesis 4.1 guarantees that a pth order RK scheme verifies the truncation error estimate

$$r^{n+1}(w) = \frac{\delta w^{n+1}}{\Delta t} + e^{n+1}(w) = C_{\mathrm{RK}}(w^n)\Delta t^p,$$

where, with the notation of Section 4.1, we have explicitly used the fact that for the last stage of the RK scheme $r^k = r^{n+1}$. Similarly, Hypothesis 4.2 ensures that the modified semi-discrete operator used in the bubble function verifies the estimate

$$\bar{r}^{n+1}(w) = \frac{\overline{\delta w^{n+1}}}{\Delta t} + e^{n+1}(w) = \overline{C}_{\mathrm{RK}}(w^n)\Delta t^l,$$

where certainly $l \leqslant p$. Both hypotheses are verified in Appendix B for the RK2 and RK3 schemes considered in the paper.

Next we define, for the stabilized Galerkin scheme, the following truncation error:

$$\mathcal{E}_n = \left| \sum_{i\in\mathcal{T}_h} \psi_i \int_\Omega \varphi_i r^{n+1}(w_h)dx\,dy + \sum_{i\in\mathcal{T}_h} \psi_i \sum_{T|i\in T} \int_T \gamma_i \overline{r^{n+1}}(w_h)dx\,dy \right|, \tag{69}$$

where the ψ_is are nodal values of a $C_0^1(\Omega)$ function, which is assumed to verify [31]

$$\|\psi\|_{L^\infty(\Omega)} \leqslant C_\psi, \|\psi_h\|_{L^\infty(\Omega)} \leqslant C_{\psi_h}; \quad \|\nabla\psi\|_{L^\infty(\Omega)} \leqslant C_{\nabla\psi}, \|\nabla\psi_h\|_{L^\infty(\Omega)} \leqslant C_{\nabla\psi_h} \tag{70}$$

having denoted by ψ_h the pth order polynomial approximation of ψ corresponding to the approximation space chosen. Similarly, w_h represents the spatial interpolant of the given smooth exact solution w. As a second step, we can immediately rewrite the error as

$$\mathcal{E}_n = \left| \overbrace{\int_\Omega \psi_h r^{n+1}(w_h) dx\,dy}^{I} + \overbrace{\sum_{T\in\mathcal{T}_h}\sum_{j\in T}\int_T \gamma_j \psi_j \overline{r^{n+1}}(w_h) dx\,dy}^{II} \right|.$$

Next we estimate the two terms in the error. For I we immediately make use of Hypothesis 4.1:

$$I = \int_\Omega \psi_h\left(\partial_t w_h^n + \nabla\cdot \boldsymbol{\mathcal{F}}_h(w_h^n)\right) dx\,dy + \int_\Omega \psi_h C_{\mathrm{RK}}(w_h^n)\Delta t^p dx\,dy.$$

Now, being w a smooth exact solution, we have $\partial_t w^n + \nabla\cdot\boldsymbol{\mathcal{F}}(u^n) = 0$, hence I can be rewritten as

$$\begin{aligned} I &= \int_\Omega \psi_h \partial_t(w_h^n - w^n) dx\,dy + \int_\Omega \psi_h \nabla\cdot\left(\boldsymbol{\mathcal{F}}_h(w_h^n) - \boldsymbol{\mathcal{F}}(w^n)\right) dx\,dy + \int_\Omega \psi_h C_{\mathrm{RK}}(w_h^n)\Delta t^p dx\,dy \\ &= \int_\Omega \psi_h \partial_t(w_h^n - w^n) dx\,dy - \int_\Omega \left(\boldsymbol{\mathcal{F}}_h(w_h^n) - \boldsymbol{\mathcal{F}}(w^n)\right)\cdot\nabla\psi_h\, dx\,dy + \int_\Omega \psi_h C_{\mathrm{RK}}(w_h^n)\Delta t^p\, dx\,dy, \end{aligned}$$

where, following [6,31], we have broken the second integral over elements, integrated by parts over each element, re-assembled, and used the fact that $\psi \in C_0^1(\Omega)$. Due to the assumptions on ψ (cf. equation (70)), we can now use the properties of the approximation to estimate all terms, ending up with

$$|I| \leqslant \mathcal{C}_w(\mathcal{T}_h, w^n)h^p + \mathcal{C}_{\boldsymbol{\mathcal{F}}}(\mathcal{T}_h, w^n)h^p + \mathcal{C}_{\mathrm{RK}}(\mathcal{T}_h, w^n)\Delta t^p = \mathcal{C}_0(\mathcal{T}_h, w^n)h^p + \mathcal{C}_{\mathrm{RK}}(\mathcal{T}_h, w^n)\Delta t^p. \tag{71}$$

This term is nothing else than the truncation error of the Galerkin scheme. As expected, it is of an order dictated purely by the spatial and temporal approximations.

We now estimate the term II. First of all we note that since $\sum_j \gamma_j = 0$, then we can write

$$II = \frac{1}{K}\sum_{T\in\mathcal{T}_h}\sum_{j\in T}\sum_{i\in T}\int_T \gamma_j(\psi_j - \psi_i)\overline{r^{n+1}}(w_h) dx\,dy,$$

where we recall that K denotes the number of DoF in an element. Next we use Hypothesis 4.2 to get

$$\begin{aligned} II = &\frac{1}{K}\sum_{T\in\mathcal{T}_h}\sum_{j\in T}\sum_{i\in T}\int_T \gamma_j(\psi_j - \psi_i)\partial_t w_h^n dx\,dy + \frac{1}{K}\sum_{T\in\mathcal{T}_h}\sum_{j\in T}\sum_{i\in T}\int_T \gamma_j(\psi_j - \psi_i)\nabla\cdot\boldsymbol{\mathcal{F}}_h(w_h^n) dx\,dy \\ &+ \frac{1}{K}\sum_{T\in\mathcal{T}_h}\sum_{j\in T}\sum_{i\in T}\int_T \gamma_j(\psi_j - \psi_i)\overline{C}_{\mathrm{RK}}(w^n)\Delta t^l dx\,dy \end{aligned}$$

Using again the fact that w is a classical solution we have

$$\begin{aligned} II = &\frac{1}{K}\sum_{T\in\mathcal{T}_h}\sum_{j\in T}\sum_{i\in T}\int_T \gamma_j(\psi_j - \psi_i)\partial_t(w_h^n - w^n) dx\,dy + \frac{1}{K}\sum_{T\in\mathcal{T}_h}\sum_{j\in T}\sum_{i\in T}\int_T \gamma_j(\psi_j - \psi_i)\nabla\cdot\left(\boldsymbol{\mathcal{F}}_h(w_h^n) - \boldsymbol{\mathcal{F}}(w^n)\right) dx\,dy \\ &+ \frac{1}{K}\sum_{T\in\mathcal{T}_h}\sum_{j\in T}\sum_{i\in T}\int_T \gamma_j(\psi_j - \psi_i)\overline{C}_{\mathrm{RK}}(w^n)\Delta t^l dx\,dy. \end{aligned}$$

In order to give an upper bound to the last expression, we make use of the fact that in 2D the total number of elements in the mesh can be bounded by h^{-2}, the properties of ψ to deduce that $\psi_j - \psi_i$ can be bounded by $\|\nabla\psi\|_{L^\infty(\Omega)}h$, the fact that $|T| \leqslant C_0 h^2$, and the properties of the approximation. This leads to

$$\begin{aligned} |II| \leqslant\ &\mathcal{C}(\Omega,\mathcal{T}_h)h^{-2}\|\gamma\|_{L^\infty(\Omega)}C_0h^2\|\nabla\psi\|_{L^\infty(\Omega)}h\mathcal{C}_w(\mathcal{T}_h,w^n)h^p + \mathcal{C}(\Omega,\mathcal{T}_h)h^{-2}\|\gamma\|_{L^\infty(\Omega)}C_0h^2\|\nabla\psi\|_{L^\infty(\Omega)}h\mathcal{C}_{\nabla\boldsymbol{\mathcal{F}}}(\mathcal{T}_h,w^n)h^{p-1} \\ &+ \mathcal{C}(\Omega,\mathcal{T}_h)h^{-2}\|\gamma\|_{L^\infty(\Omega)}C_0h^2\|\nabla\psi\|_{L^\infty(\Omega)}h\overline{C}_{\mathrm{RK}}(w^n)\Delta t^l. \end{aligned}$$

With $\|\gamma\|_{L^\infty(\Omega)} = \max_{T\in\mathcal{T}_h}\max_{j\in T}\|\gamma_j\|_{L^\infty(T)}$. Setting $\mathcal{C}_1(\Omega,\mathcal{T}_h,w^n) = \mathcal{C}(\Omega,\mathcal{T}_h)C_0C_{\nabla\psi}\max(\mathcal{C}_w(\mathcal{T}_h,w^n),\mathcal{C}_{\nabla\boldsymbol{\mathcal{F}}}(\mathcal{T}_h,w^n))$, and $\overline{\mathcal{C}}_{\mathrm{RK}}(\Omega,\mathcal{T}_h,w^n) = \mathcal{C}(\Omega,\mathcal{T}_h)C_0C_{\nabla\psi}\overline{C}_{\mathrm{RK}}(w^n)$ we get the estimate

$$|II| \leqslant \|\gamma\|_{L^\infty(\Omega)}\left(\mathcal{C}_1(\Omega,\mathcal{T}_h,w^n)h^p + \overline{\mathcal{C}}_{\mathrm{RK}}(\Omega,\mathcal{T}_h,w^n)h\Delta t^l\right).$$

Assembling the Galerkin error and the error associated to the bubble, we get finally

$$\mathcal{E}_n \leqslant \mathcal{C}_0(\mathcal{T}_h,w^n)h^p + \mathcal{C}_{\mathrm{RK}}(\mathcal{T}_h,w^n)\Delta t^p + \|\gamma\|_{L^\infty(\Omega)}\mathcal{C}_1(\Omega,\mathcal{T}_h,w^n)h^p + \|\gamma\|_{L^\infty(\Omega)}\overline{\mathcal{C}}_{\mathrm{RK}}(\Omega,\mathcal{T}_h,w^n)h\Delta t^l. \tag{72}$$

This immediately shows that, provided that the bubble functions are uniformly bounded, we are allowed to have $l \leqslant p$, in particular, it is enough to take $l = p - 1$ to retain the accuracy of the Galerkin approximation.

In particular, if, as it is always the case for explicit schemes, we can find two positive bounded constants $C_{h/\Delta t}$ and $C_{\Delta t/h}$ such that

$$C_{h/\Delta t} \leqslant \frac{\Delta t}{h} \leqslant C_{\Delta t/h}$$

then we have for $l = p - 1$

$$\mathcal{E}_n \leqslant \mathcal{C} h^p \tag{73}$$

with

$$\mathcal{C} = \mathcal{C}_0(\mathcal{T}_h, w^n) + \mathcal{C}_{\mathrm{RK}}(\mathcal{T}_h, w^n) C^p_{\Delta t/h} + \|\gamma\|_{L^\infty(\Omega)} \left(\mathcal{C}_1(\Omega, \mathcal{T}_h, w^n) + \overline{\mathcal{C}}_{\mathrm{RK}}(\Omega, \mathcal{T}_h, w^n) C^{p-1}_{\Delta t/h} \right).$$

Note that, mass lumping is kept out of the analysis. However, as shown in Section 3, it can be included in the definition of the (bounded) bubble function, at least in the P^1 case. For the higher order case, we refer to [23,39,38] for more.

Appendix B. Hypotheses 4.1 and 4.2

In this appendix, we justify the choice of the approximate time increments $\overline{\delta u^k}$ (cf. Section 4.1 and Appendix A) for the RK2 and RK3 schemes of Section 4.1. We recall that the constraint to respect is that for the last RK step

$$\bar{r}^k = \frac{\overline{\delta u^k}}{\Delta t} + \bar{e}^k = \mathcal{O}(\Delta t^l)$$

with $l \geqslant p - 1$, where with p we denote the (desired) overall accuracy of the scheme. The analysis will be performed for the autonomous ODE:

$$\partial_t u + e(u) = 0. \tag{74}$$

B.1. RK2 scheme

Let us start by verifying Hypothesis 4.1 for the RK2 scheme defined by

$$\begin{aligned} u^1 &= u^n - \Delta t e(u^n), \\ u^{n+1} &= u^n - \frac{\Delta t}{2} e(u^n) - \frac{\Delta t}{2} e(u^1). \end{aligned}$$

When replacing u^n and u^{n+1} by the values at t^n and t^{n+1} of an exact solution $w(t)$, and using the fact that $w^1 = w^n - \Delta t f(w^n)$, we can write

$$\begin{aligned} e(w^1) &= e(w^n + (w^1 - w^n)) = e(w^n) + (w^1 - w^n)\partial_u e(u^n) + \frac{(w^1 - w^n)^2}{2} \partial_{uu} e(u^n) + \mathcal{O}((w^1 - w^n)^3) \\ &= e(w^n) - \Delta t e(u^n) \partial_u e(u^n) + \frac{\Delta t^2}{2} e(u^n)^2 \partial_{uu} e(u^n) + \mathcal{O}(\Delta t^3) \end{aligned}$$

which immediately leads to

$$\begin{aligned} \frac{w^{n+1} - w^n}{\Delta t} + \frac{1}{2}(e(w^n) + e(w^1)) &= \partial_t w^n + \frac{\Delta t}{2} \partial_{tt} w^n + \frac{\Delta t^2}{6} \partial_{ttt} w^n + e(w^n) - \frac{\Delta t}{2} e(w^n) \partial_u e(w^n) + \frac{\Delta t^2}{4} e(w^n)^2 \partial_{uu} e(w^n) + \mathcal{O}(\Delta t^3) \\ &= \partial_t w^n + e(w^n) - \frac{\Delta t^2}{3} \left(\frac{1}{2} e(w^n) \partial_u e(w^n)^2 + \frac{1}{4} e(w^n)^2 \partial_{uu} e(w^n) \right) + \mathcal{O}(\Delta t^3) = \mathcal{O}(\Delta t^2) \end{aligned}$$

having used the relations

$$\begin{aligned} &\partial_t w^n = -e(w^n), \\ &\partial_{tt} w^n = e(w^n) \partial_u e(w^n), \\ &\partial_{ttt} w^n = -e(w^n) \partial_u e(w^n)^2 - e(w^n)^2 \partial_{uu} e(w^n), \\ &\partial_{tttt} w^n = e(w^n) \partial_u e(w^n)^3 + 4 e(w^n)^2 \partial_u e(w^n) \partial_{uu} e(w^n) + e(w^n)^3 \partial_{uuu} e(w^n). \end{aligned} \tag{75}$$

To verify Hypothesis 4.2, we perform a similar exercise:

$$\begin{aligned} \bar{r}^{n+1} &= \frac{w^1 - w^n}{\Delta t} + \frac{1}{2}(e(w^n) + e(w^1)) = -e(w^n) + \frac{1}{2}(e(w^n) + e(w^1)) = -\frac{1}{2} e(w^n) + \frac{1}{2} e(w^n) - \frac{\Delta t}{2} e(w^n) \partial_u e(w^n) + \mathcal{O}(\Delta t^2) \\ &= -\frac{\Delta t}{2} e(w^n) \partial_u e(w^n) + \mathcal{O}(\Delta t^2) = \mathcal{O}(\Delta t) \end{aligned}$$

proving that this definition of $\bar{r}^{n+1}$ is enough for use in the stabilization term in second order schemes.

B.2. RK3 scheme

We repeat the same exercise for the RK3 scheme defined by

$$u^1 = u^n - \Delta t e(u^n),$$
$$u^2 = u^n - \frac{\Delta t}{4} e(u^n) - \frac{\Delta t}{4} e(u^1),$$
$$u^{n+1} = u^n - \frac{\Delta t}{6} e(u^n) - \frac{2\Delta t}{3} e(u^2) - \frac{\Delta t}{6} e(u^1).$$

When replacing u^n and u^{n+1} by the values at t^n and t^{n+1} of an exact solution $w(t)$, we can easily prove the following developments

$$\begin{aligned} e(w^1) &= e(w^n) - \Delta t e(w^n)\partial_u e(w^n) + \frac{\Delta t^2}{2} e(w^n)^2 \partial_{uu} e(w^n) - \frac{\Delta t^3}{6} e(w^n)^3 \partial_{uuu} e(w^n) + \mathcal{O}(\Delta t^4) e(w^2) \\ &= e(w^n) - \frac{\Delta t}{2} e(w^n)\partial_u e(w^n) + \frac{\Delta t^2}{4}\left(e(w^n)\partial_u e(w^n)^2 + \frac{1}{2} e(w^n)^2 \partial_{uu} e(w^n)\right) \\ &\quad - \frac{\Delta t^3}{8}\left(2e(w^n)^2 \partial_u e(w^n)\partial_{uu} e(w^n) + \frac{1}{6} e(w^n)^3 \partial_{uuu} e(w^n)\right) + \mathcal{O}(\Delta t^4) \end{aligned}$$

These developments can be readily used to show that

$$\begin{aligned} \frac{w^{n+1} - w^n}{\Delta t} + \frac{1}{6} e(w^n) + \frac{1}{6} e(w^1) + \frac{2}{3} e(w^2) &= \partial_t w^n + \frac{\Delta t}{2}\partial_{tt} w^n + \frac{\Delta t^2}{6}\partial_{ttt} w^n + \frac{\Delta t^3}{24}\partial_{tttt} w^n + \frac{1}{6} e(w^n) + \frac{1}{6} e(w^n) \\ &\quad - \frac{\Delta t}{6} e(w^n)\partial_u e(w^n) + \frac{\Delta t^2}{12} e(w^n)^2 \partial_{uu} e(w^n) - \frac{\Delta t^3}{36} e(w^n)^3 \partial_{uuu} e(w^n) + \frac{2}{3} e(w^n) \\ &\quad - \frac{\Delta t}{3} e(w^n)\partial_u e(w^n) + \frac{\Delta t^2}{6}\left(\frac{1}{2} e(w^n)^2 \partial_{uu} e(w^n) + e(w^n)\partial_u e(w^n)^2 \right) \\ &\quad - \frac{\Delta t^3}{12}\left(2e(w^n)^2 \partial_u e(w^n)\partial_{uu} e(w^n) + \frac{1}{6} e(w^n)^3 \partial_{uuu} e(w^n)\right) + \mathcal{O}(\Delta t^4) \end{aligned}$$

which, using (75), leads immediately to

$$\frac{w^{n+1} - w^n}{\Delta t} + \frac{1}{6} e(w^n) + \frac{1}{6} e(w^1) + \frac{2}{3} e(w^2) = \partial_t w^n + e(w^n) + \frac{\Delta t^3}{12} e(w^n)\partial_u e(w^n)^3 + \mathcal{O}(\Delta t^4) = \mathcal{O}(\Delta t^3)$$

A similar exercise can be used now to show that

$$\begin{aligned} \bar{r}^2(w) &= \frac{w^1 - w^n}{2\Delta t} + \frac{1}{4} e(w^n) + \frac{1}{4} e(w^1) = -\frac{1}{2} e(w^n) + \frac{1}{4} e(w^n) + \frac{1}{4} e(w^n) - \frac{\Delta t}{4} e(w^n)\partial_u e(w^n) + \mathcal{O}(\Delta t^2) \\ &= -\frac{\Delta t}{4} e(w^n)\partial_u e(w^n) + \mathcal{O}(\Delta t^2) = \mathcal{O}(\Delta t) \end{aligned}$$

and more importantly that

$$\begin{aligned} \bar{r}^{n+1}(w) &= 2\frac{w^2 - w^n}{\Delta t} + \frac{1}{6} e(w^n) + \frac{1}{6} e(w^1) + \frac{2}{3} e(w^2) \\ &= \frac{2}{\Delta t}\left(-\frac{\Delta t}{2} e(w^n) + \frac{\Delta t^2}{4} e(w^n)\partial_u e(w^n) - \frac{\Delta t^3}{8} e(w^n)^2 \partial_{uu} e(w^n)\right) + \frac{1}{6} e(w^n) + \frac{1}{6} e(w^n) - \frac{\Delta t}{6} e(w^n)\partial_u e(w^n) \\ &\quad + \frac{\Delta t^2}{12} e(w^n)^2 \partial_{uu} e(w^n) + \frac{2}{3} e(w^n) - \frac{\Delta t}{3} e(w^n)\partial_u e(w^n) + \frac{\Delta t^2}{6}\left(e(w^n)\partial_u e(w^n)^2 + \frac{1}{2} e(w^n)^2 \partial_{uu} e(w^n)\right) + \mathcal{O}(\Delta t^3) \\ &= \frac{\Delta t^2}{6}\left(e(w^n)\partial_u e(w^n)^2 - \frac{1}{2} e(w^n)^2 \partial_{uu} e(w^n)\right) + \mathcal{O}(\Delta t^3) = \mathcal{O}(\Delta t^2) \end{aligned}$$

which shows that also for the RK3 scheme, our definitions of the $\bar{r}^k$ do verify the accuracy constraint.

References

[1] R. Abgrall, Toward the ultimate conservative scheme: following the quest, J. Comput. Phys. 167 (2) (2001) 277–315.
[2] R. Abgrall, Essentially non oscillatory residual distribution schemes for hyperbolic problems, J. Comput. Phys. 214 (2) (2006) 773–808.
[3] R. Abgrall, Residual distribution schemes: current status and future trends, Comput. Fluids 35 (7) (2006) 641–669.
[4] R. Abgrall, M. Mezine, Construction of second order accurate monotone and stable residual distribution schemes for unsteady flow problems, J. Comput. Phys. 188 (2003) 16–55.
[5] R. Abgrall, M. Mezine, Construction of second-order accurate monotone and stable residual distribution schemes for steady flow problems, J. Comput. Phys. 195 (2004) 474–507.

[6] R. Abgrall, P.L. Roe, High order fluctuation schemes on triangular meshes, J. Sci. Comput. 19 (3) (2003) 3–36.
[7] R. Abgrall, C.W. Shu, Development of residual distribution schemes for the discontinuous Galerkin method: the scalar case with linear elements, Commun. Comput. Phys. 5 (2009) 376–390.
[8] C. Bolley, M. Crouzeix, Conservation de la positivité lors de la discétization des problèmes d'èvolution paraboliques, R.A.I.R.O. Anal. Numer. 12 (1978) 237–254.
[9] D. Caraeni, L. Fuchs, Compact third-order multidimensional upwind scheme for Navier Stokes simulations, Theor. Comput. Fluid Dynam. 15 (2002) 373–401.
[10] D.A. Caraeni, Development of a Multidimensional Upwind Residual Distribution Solver for Large Eddy Simulation of Industrial Turbulent Flows, Ph.D. Thesis, Lund Institute of Technology, 2000.
[11] C. Corre, X. Du, A residual-based scheme for computing compressible flows on unstructured grids, Comput. Fluids 38 (7) (2009) 1338–1347.
[12] C.-S. Chou, C.-W. Shu, High order residual distribution conservative finite difference Weno schemes for steady state problems on non-smooth meshes, J. Comput. Phys. 214 (3) (2006) 698–724.
[13] B. Cockburn, C.W. Shu, The Runge Kutta discontinuous Galerkin method for conservation laws V: Multidimensional systems, J. Comput. Phys. 141 (2) (1998) 199–224.
[14] C. Corre, G. Hanss, A. Lerat, A residual-based compact scheme for the unsteady compressible Navier–Stokes equations, Comput. Fluids 34 (4–5) (2005) 561–580.
[15] Á. Csík, H. Deconinck, Space time residual distribution schemes for hyperbolic conservation laws on unstructured linear finite elements, Int. J. Numer. Methods Fluids 40 (2002) 573–581.
[16] Á. Csík, M. Ricchiuto, H. Deconinck, A conservative formulation of the multidimensional upwind residual distribution schemes for general nonlinear conservation laws, J. Comput. Phys. 179 (2) (2002) 286–312.
[17] Á. Csík, M. Ricchiuto, H. Deconinck, S. Poedts, Space-time residual distribution schemes for hyperbolic conservation laws, in: 15th AIAA Computational Fluid Dynamics Conference, Anahein, CA, USA, June 2001.
[18] H. Deconinck, M. Ricchiuto, Residual distribution schemes: foundation and analysis, in: E. Stein, R. de Borst, T.J.R. Hughes (Eds.), Encyclopedia of Computational Mechanics, John Wiley & Sons, Ltd., 2007, doi:10.1002/0470091355.ecm054.
[19] H. Deconinck, K. Sermeus, R. Abgrall, Status of multidimensional upwind residual distribution schemes and applications in aeronautics, in: AIAA Paper 2000-2328, AIAA CFD Conference, Denver USA, June 2000.
[20] P. DePalma, G. Pascazio, G. Rossiello, M. Napolitano, A second-order accurate monotone implicit fluctuation splitting scheme for unsteady problems, J. Comput. Phys. 208 (1) (2005) 1–33.
[21] J. Dobes, H. Deconinck, Second order blended multidimensional upwind residual distribution scheme for steady and unsteady computations, J. Comput. Appl. Math. 215 (1) (2006) 378–389.
[22] A. Ferrante, H. Deconinck, Solution of the Unsteady Euler Equations Using Residual Distribution and Flux Corrected Transport, Technical Report VKI-PR 97-08, von Karman Institute for Fluid Dynamics, 1997.
[23] G. Cohen, P. Joly, J.E. Roberts, N. Tordjman, High order triangular finite elements with mass lumping for the wave equation, SIAM J. Numer. Anal. 38 (6) (2001) 2047–2078.
[24] G. Hauke, M.H. Doweidar, Fourier analysis of semi-discrete and space time stabilized methods for the advective diffusive reactive equation: I. SUPG, Comput. Methods Appl. Mech. Eng. 194 (1) (2005) 45–81.
[25] G. Hauke, M.H. Doweidar, Fourier analysis of semi-discrete and space time stabilized methods for the advective diffusive reactive equation: II. SGS, Comput. Methods Appl. Mech. Eng. 194 (6-8) (2005) 691–724.
[26] G. Hauke, M.H. Doweidar, Fourier analysis of semi-discrete and space time stabilized methods for the advective diffusive reactive equation: III. SGS/GSGS, Comput. Methods Appl. Mech. Eng. 195 (44–47) (2006) 6158–6176.
[27] M. Hubbard, Discontinuous fluctuation distribution, J. Comput. Phys. 227 (24) (2008) 10125–10147.
[28] T.J.R. Hughes, T.E. Tezduyar, Development of time-accurate finite element techniques for first order hyperbolic systems with emphasis on the compressible euler equations, Comput. Methods Appl. Mech. Eng. 45 (1–3) (1984) 217–284.
[29] J. Maerz, G. Degrez, Improving Time Accuracy of Residual Distribution Schemes, Technical Report VKI-PR 96-17, von Karman Institute for Fluid Dynamics, 1996.
[30] M. Ricchiuto, R. Abgrall, Stable and convergent residual distribution for time-dependent conservation laws, in: ICCFD4 Proceedings, Springer-Verlag, 2006.
[31] M. Ricchiuto, R. Abgrall, H. Deconinck, Application of conservative residual distribution schemes to the solution of the shallow water equations on unstructured meshes, J. Comput. Phys. 222 (2007) 287–331.
[32] M. Ricchiuto, A. Bollermann, Stabilized residual distribution for shallow water simulations, J. Comput. Phys. 228 (4) (2009) 1071–1115.
[33] M. Ricchiuto, Á. Csík, H. Deconinck, Residual distribution for general time dependent conservation laws, J. Comput. Phys. 209 (1) (2005) 249–289.
[34] P.L. Roe, Fluctuations and signals – a framework for numerical evolution problems, in: K.W. Morton, M.J. Baines (Eds.), Numerical Methods for Fluids Dynamics, Academic Press, 1982, pp. 219–257.
[35] G. Rossiello, P. DePalma, G. Pascazio, M. Napolitano, Second-order-accurate explicit fluctuation splitting schemes for unsteady problems, Comput. Fluids 38 (7) (2009) 384–1393.
[36] G. Scovazzi, E. Love, M.J. Shashkov, Multi-scale Lagrangian shock hydrodynamics on q1/p0 finite elements: theoretical framework and two-dimensional computations, Comput. Methods Appl. Mech. Eng. 197 (9–12) (2007) 056–1079.
[37] F. Shakib, T.J.R. Hughes, A new finite element formulation for computational fluid dynamics: IX. Fourier analysis of space–time Galerkin/least-squares algorithms, Comput. Methods Appl. Mech. Eng. 87 (1) (1991) 35–58.
[38] S. Jund, Méthodes d'éléments finis d'ordre élevé pour la simulations numérique de la propagation d'ondes, Ph.D. Thesis, Université Lous Pasteur, Strasbourg, 2007.
[39] S. Jund, S. Salmon, Arbitrary high order finite element schemes and high order mass lumping, Int. J. Appl. Math. Comput. Sci. 17 (3) (2007) 375–393.
[40] T.E. Tezduyar, T.J.R. Hughes, Development of Time-Accurate Finite Element Techniques for First Order Hyperbolic Systems With emphasis on the Compressible Euler Equations, Technical Report NASA-CR-204772, NASA-Ames, 1983.
[41] Z.J. Wang, Laiping Zhang, Yen Liu, Spectral (finite) volume method for conservation laws on unstructured grids IV: Extension to two-dimensional systems, J. Comput. Phys. 194 (2) (2004) 16–741.
[42] P.R. Woodward, P. Colella, The numerical simulation of two-dimensional flows with strong shocks, J. Comput. Phys. 54 (1984) 115–173.